Damage Characterization of Adhesively-Bonded Bi-material Joints using Acoustic Emission

Milad Saeedifar[1], Mohamed Nasr Saleh, Sofia Teixeira De Freitas, Dimitrios Zarouchas

Structural Integrity & Composites Group, Faculty of Aerospace Engineering, Delft University of Technology, The Netherlands.

Abstract

The aim of the present study is to characterize the damage in bi-material steel-to-composite double-lap adhesively-bonded joints using Acoustic Emission (AE). Two different structural adhesives, a ductile (Methacrylate-based) and brittle (Epoxy-based), were used to bond CFRP skins to a steel core. The fabricated joints were loaded in tension while damage evolution was monitored by AE. Due to the difference in the fracture nature of the adhesives "ductile vs. brittle", different damage mechanisms were observed; including cohesive failure within the adhesive layer, steel deformation, failure at the adhesive/adherends interface (adhesive failure) and delamination in the CFRP skin. To classify these damages by AE, the AE features of each damage mechanism were first obtained by conducting standard tests on the individual constituents. Then, these AE reference patterns were used to train an ensemble decision tree classifier. The best parameters of the ensemble model were obtained by Bayesian optimization, and the confusion matrix showed that the model was sufficiently trained with the accuracy of 99.5% and 99.8% for Methacrylate-based and Epoxy-based specimens respectively. Afterwards, the trained model was used to classify the AE signals of the double-lap specimens. The AE demonstrated that the dominant damage mechanisms in the case of the Methacrylate-based were cohesive and adhesive failures while in the case of the Epoxy-based they were CFRP skin failure and adhesive failure. These results were consistent with the Digital Image Correlation, Fiber Optic Sensor and camera results. This study demonstrates the potential of AE technique for damage characterization of adhesively-bonded bi-material joints.

[1] Corresponding Author: M Saeedifar (m.saeedifar@tuedlft.nl)

Keywords: B. Adhesion; C. Damage mechanics; D. Acoustic emission; E. Joints/joining; Supervised classification.

1 Introduction

The use of adhesively-bonded joints is preferred over conventional joining techniques such as bolting, riveting and welding. They offer many advantages including, for instance, the ability to join dissimilar materials such as steel and fiber reinforced composites, weight savings, improved stress distribution along the bond-line and enhancement of the corrosion and fatigue resistance characteristics [1-3] which are essential, especially in maritime applications.

However, the dominant damage mechanisms in these joints may vary based on various factors including: loading conditions, environmental conditions, mechanical properties of adhesive and adherends and also the adhesion quality between adhesive and adherends. These damage mechanisms include, but are not limited to: interfacial failure between the adherends and adhesive layer (i.e., adhesive failure), cohesive failure within the adhesive layer and the failure within the adherends [4-5]. Heshmati et al. [6-9] did extensive experimental and numerical studies to investigate the effect of environmental conditions, like moisture, temperature, de-icing salt solution and cyclic loading, on the durability and the damage mechanisms of adhesively-bonded FRP/steel joints. The results showed that the joint strength is a function of the dominant failure mode of the joint which varied under different environmental conditions. Thus, a deep and thorough understanding of the fracture behavior of the bi-material adhesively-bonded joints is essential to fully utilize their capabilities in industrial applications. Thanks to the successful performance of Non-Destructive Evaluation

(NDE) techniques for damage assessment in the engineering structures, they can be good candidates for damage characterization in such joints.

Among the NDE techniques, Acoustic Emission (AE) provides attractive capabilities for online detection, classification and localization of damage in engineering structures [10-12], and it is a good candidate for the monitoring of the damage process of adhesively-bonded structures. However, due to the presence of different constituents as well as the interfaces in the adhesively-bonded bi-material joints, AE-based detection and classification of different damage mechanisms of these joints is still a challenging task. Lee et al. [13] studied the damage evolution in Double-Lap Joint (DLJ) specimens fabricated from a CFRP core bonded to two steel skins by three different approaches including adhesive bonding, mechanical bonding and adhesive/mechanical hybrid bonding. They used a high-speed camera and AE to detect the failure of adhesive and mechanical bonding. The results showed that AE could distinguish the adhesive bonding failure from the mechanical bonding failure. Fotouhi et al. [14] monitored different damage mechanisms in a sandwich structure containing a foam core adhesively-bonded to two GFRP skins by AE. They managed to distinguish and classify four different damage mechanisms in the sandwich specimens by analyzing AE data using wavelet packet transform method. These damage mechanisms were: foam core failure, adhesive layer failure, matrix cracking and fiber breakage in the GFRP skin. Xu et al. [15] identified damage modes in adhesively-bonded composite single lap joints by means of AE and k-Means++ unsupervised clustering methods. The results showed that the adhesive layer failure, matrix cracking, fiber/matrix debonding and fiber breakage had the lowest to highest frequency bands respectively. Kupski et al. [16] investigated the fracture of adhesively-bonded CFRP single lap joints by AE and Finite Element Modelling (FEM). In their study,

AE was employed successfully to detect the initiation of damage in the specimens. Nevertheless to the best of the authors' knowledge there are just a few studies on the damage assessment of adhesively-bonded bi-material joints by AE, and most of them used the unsupervised clustering and signal processing methods to classify damage mechanisms. The performance of these methods is not acceptable when the AE signals of damages are not clearly distinguishable and there are considerable overlaps between the AE features of different damages [17, 18].

This research represents a step towards "Establishing an Structural Health Monitoring (SHM) methodology for enabling qualification of bi-material joints for lightweight and safe maritime transport". Fig. 1 shows the general framework for this research. To achieve this objective, SHM methodology needs first to be well-established for the test coupons level. It is, then, validated for the subcomponent level and finally, implemented for the full-scale structure. Therefore, this study is devoted only to the pyramid base tests, i.e. test coupons level and other test levels are out of the scope. Thus, this paper deals with the damage characterization of a double-lap bi-material joint, bonded with a thick adhesive, by supervised classification of AE signals. The DLJ test coupons are designed in a way to simulate the stress condition that the real bi-material joint is experiencing in the full-scale ship structure. The flowchart of the damage characterization process proposed in the present study is shown in Fig. 2. In order to distinguish and classify the different damage mechanisms observed in the DLJ specimens, the AE signatures of each damage mechanism were obtained by conducting standard tests on the individual constituent materials of the joint. These AE signatures were then used to train an ensemble decision tree classifier. Finally, the trained classifier was employed to classify different damage mechanisms in the DLJ specimens and

the AE results were validated against results obtained from Digital Image Correlation (DIC), Fiber Optic Sensor (FOS) and camera images.

2 Materials and manufacturing

2.1 Adherends and Adhesives

The steel used in this study is high strength structural shipbuilding steel AH36 with the mechanical properties listed in Table 1. The CFRP laminates are produced using vacuum infusion. In order to avoid galvanic corrosion, a thin layer of chopped glass fiber fabric was used on both sides. The lay-up was [glass/0/90/45/-45]$_S$ with the 0º-direction in the length direction of the final specimen geometry.

The first adhesive used to bond the steel and CFRP adherends was a two-component Methacrylate adhesive (MMA-based) with a mixing ratio of 10:1 by volume. The second adhesive used was a two-component toughened Epoxy adhesive (Epoxy-based) with a mixing ratio of 2:1 by volume. The mechanical properties of the both adhesive types are listed in Table 1.

2.2 Joint design and manufacturing

The DLJ specimen consists of two steel cores separated by a Teflon insert of 1 mm thick and bonded with thick adhesive layers (8 mm) to CFRP skins as depicted in Fig. 3.

3 Experimental Procedures

3.1 Test Procedure

The testing setup shown in Fig. 4, consists of five main data acquisition systems. The Universal Testing Machine (UTM) records the load and the cross-head displacement. The corresponding displacement and the strain contour measurements are acquired by processing

in-situ images captured by a 3D Digital Image Correlation (DIC) system from one side. A camera continuously monitors the cross-section of the specimen during the loading process from the opposite side. A Fiber Optic Sensor (FOS), attached on one CFRP skin of specimen, records the strain distribution on the specimen skin. Finally, the AE sensor placed on the specimen surface is used to capture the AE activities of the specimen during the loading process. Tensile testing was conducted in accordance with ASTM D3528 standard [19]. Universal Testing Machine (Zwick Roell) with 250 kN load cell is used to apply a displacement controlled tension with a rate of 1.27 mm/min according to the standard. The displacement controlled mode is used to reduce the effect of varying the adhesive thickness on the coupons' response [20]. Three specimens are tested for each adhesive type.

3.2 In-situ monitoring apparatus

In this section, different in-situ monitoring apparatus used during the DLJ tests are presented.

3.2.1 Acoustic emission

In order to capture the generated AE signals during the tests, one AE sensor was placed on the specimen (see Fig. 4). It is worth mentioning that at the beginning of the test, four AE sensors were used to capture the AE signals; two were mounted on the CFRP skin and two on the steel. However, due to the catastrophic fracture with sudden energy release of the Epoxy-based adhesive specimens, only one sensor was used on the steel to avoid any damage of the AE sensors for all the consecutive tests. For consistency of the analysis, only the AE signals recorded by the sensor mounted on the steel is used for all the specimens. Some literature [21-23] reported the effect of some parameters like material properties and surface roughness on the attenuation of the AE wave. To investigate the wave attenuation in

the bi-material joint, a pencil lead breakage test was performed at the middle of DLJ specimen, and it was found that the AE sensor which was placed on the steel core at the distance of 200 mm from the AE source could record the AE signal with 20 dB higher amplitude in comparison to the AE sensor mounted on the CFRP skin at the distance of 100 mm from the AE source. The obtained results showed that the attenuation of the wave in CFRP skin is much higher than the steel core. This ensures that AE signals originated from the CFRP skin or the adhesive layer will not be missed by using only one AE sensor placed on the steel core instead of four sensors.

The AE sensor was a broadband, resonant-type, and single-crystal piezoelectric transducer from Vallen Systeme GmbH, AE1045S-VS900M, with external 34 dB pre-amplifier and an operating frequency range of [100–900 kHz]. As previously highlighted, this study is the first step toward implementation of AE in the real ship structure. Due to the existence of environmental noises, usually caused by the sea environment and propulsion system, setting low threshold values may result in capturing a lot of noise signals. Thus, the AE threshold for the DLJ tests was set to 50 dB to resemble the same threshold level that the actual SHM system has to operate at. An AMSY-6 Vallen, 8-channel acoustic emission system with the sampling rate of 2 MHz, was used to record the AE signals. Ultrasound gel was applied between the surfaces of the sensor and the specimen to ensure good acoustical coupling. A standard pencil lead break procedure [24] was used to check the connection between the specimen and the AE sensor surface prior to the mechanical test.

3.2.2 Fiber optic sensor

FOS was employed to measure the strain along the CFRP skin. The FOS consisted of three different sections: LC/APC connector, the measuring section and the coreless section

to minimize back reflections and reduces power density at the fiber end. The measuring section is a Graded-Index Multimode (GIMM) fiber with core/cladding diameter of 50/125 μm produced by Plasma Optical Fibre Inc. The end coreless section, which was spliced to the measuring section, is a solid silica glass rod with an acrylate coating with diameter of Ø125 μm produced by THORLABS Inc. An ODiSL-B system from Luna Innovations Inc., which works based on the Rayleigh Backscattering theory, was used to measure the strain along the fiber length by intervals of 0.65 mm and a sampling rate of 23.8 Hz. The FOS was glued to the CFRP skin following the desired path (see Fig. 5). Three segments are then specified to capture the strain distribution at the CFRP skin along these lines.

3.2.3 Digital image correlation

The DIC system used for the full-field strain measurement consists of two 8-bit "Point Grey" cameras with "XENOPLAN 1.4/23" lenses. Both cameras have a resolution of 5 MP. Vic-Snap 8 software was used to record the speckle pattern images from the cameras, and the 3D DIC system was calibrated before the testing. The acquisition frame rate was set to 3 frames per second (fps) for the uniaxial tensile testing. The speckle pattern images acquired by Vic-Snap 8 were then processed using Vic-3D 8 software. In processing these images, the subset size was set to 21 x 21 pixels with a step size (distance between subsets) of 7 pixels. The observation window of approximately (600 x 30) mm^2 produced an image with dimensions of (2048 x 102) pixels. Global mean values of strains ($\varepsilon_{xx};\varepsilon_{yy};\varepsilon_{xy}$) are obtained from DIC analysis using Vic-3D 8 software.

4 Ensemble Bagged Tree Classifier

The unsupervised clustering techniques usually exhibit some level of blindness in the clustering process, and accordingly they cannot realize the actual intrinsic structure of data [17, 18]. Moreover, the output from the unsupervised clustering techniques is only the grouped data without any labels, which means that assigning the correct label to the grouped data will still be a challenge. Therefore, if well-known labeled data is available, unsupervised clustering is not an effective tool for meaningful discrimination of data sets anymore. In this case, supervised classification is an appropriate technique to obtain the meaningful information on the data structure [18, 25-26]. Generally, there are two steps in the supervised classification: 1) Training, and 2) Prediction. In the first step, the classifier is trained by a dataset consisting of n data; d_1, d_2, …, d_n; in which each data (d_i) has m features; p_1, p_2, …, p_m. These data are labelled already with the a set of labels (C) consisting of c_1, c_2, …, c_k, where c_i shows the class number i, and k is the total number of classes. In the prediction phase, the classifier assigns a specific class (label) to a new fed data.

Decision tree is one of the most popular classification methods that provides good interpretability, acceptable accuracy and low computational cost. In addition, the performance of decision trees significantly increases when they are combined with ensemble methods [27]. The ensemble bagged tree classifier used in the present study blends several CART decision trees [28] to get a better functionality in comparison with one decision tree. It divides the original training dataset to several subsets. Then a random combination of some subsets is selected to train a specific decision tree and it continues until all trees be trained. In the prediction phase, the classifier assigns a specific class (label) to a new fed data which the assigned class is one that results in the highest weighted average of the posterior

probability computed using the selected trees. For each class $c \in C$ and each tree; $t = 1, 2, ..., T$; the posterior probability ($p_t(c|d)$) of class c, given data d, using tree t is calculated as:

$$p_t(c|d) = \frac{p_t(d|c)p(c)}{p(d)} \tag{1}$$

If S is considered as the set of indices of selected trees involved in the class prediction of data d, the weighted average of the class posterior probabilities over the selected trees is then calculated as [29]:

$$p_{Bagged}(c|d) = \frac{\sum_{t=1}^{T} \alpha_t p_t(c|d) I(t \in S)}{\sum_{t=1}^{T} \alpha_t I(t \in T)} \tag{2}$$

where $I(t \in T)$ is 1 if t is in the set S, and 0 otherwise, and α_t is the weight of tree t. Finally, the predicted class ($PC_{Bagged}(c|d)$) for data d is the class that yields the largest weighted average [29]:

$$PC_{Bagged}(c|d) = \underset{c \in C}{\arg max}\{p_{Bagged}(c|d)\} \tag{3}$$

5 Results and Discussion

The results are presented in two subsections. The first one presents the load-displacement curves of the DLJ specimens and then the in-situ monitoring results are discussed in the second.

5.1 Mechanical results

The load-displacement curves of the DLJ specimens are depicted in Fig. 6. The load-displacement response of the MMA-based DLJ specimens has a nonlinear behavior from the beginning of the test up to the final failure with a significant plasticity and damage progression leading to a ductile fracture. On the contrary, the load-displacement response for the Epoxy-based DLJ specimens is almost linear up to the final failure, which can be described as a brittle fracture. It is clear from the load-displacement data that there is a trade-off between the strength and the ductility "displacement to failure" of the DLJ specimens. In the case of the DLJ specimen manufactured by MMA-based adhesive, the displacement to failure is approximately 4 times higher than the Epoxy-based DLJ specimen; while the strength of the Epoxy-based DLJ specimen is almost 1.6 times higher than the MMA-based one.

The fractured specimens are shown in Fig. 7. As expected, different damage mechanisms can be spotted for the two types of specimens. For the MMA-based specimens (see Fig. 7(a)), the dominant damage mechanisms are plastic deformation and crack growth in the adhesive material (cohesive failure). In addition, some adhesive failure at the steel/adhesive interface can be spotted in the middle of the specimen, where the notch is, and at the upper and lower free edges. In addition, no delamination is observed in the CFRP skin. Finally, there is infinitesimal adhesive failure at the CFRP/adhesive interface at the middle of the specimen where the crack in the adhesive material reaches the CFRP/adhesive interface.

In the case of Epoxy-based specimens (see Fig. 7(b)), there is a complete adhesive failure at the steel/adhesive interface and also a large interlaminar delamination in the CFRP

skin. Moreover, some clear transverse cracks are seen in the adhesive. In order to deeply understand the damage process up to fracture, the in-situ monitoring results are detailed in the following subsection.

5.2 In-situ monitoring results

The AE activities of the DLJ specimens under tensile loading were captured by the AE sensor mounted on the surface of the specimens. Figs. 8 and 9 show the load and AE frequency versus the displacement for both types of specimens. There is no AE event for both specimens at the beginning of loading which indicates there is no damage in the DLJ specimens. The camera images taken from the DLJ specimens also do not show any detectable damage in the specimens in this region (see Figs. 8(b) and 9(b)). The AE events of MMA-based specimen start at the displacement of 2.5 mm approximately, where a few AE events were captured with a frequency less than 150 kHz. The image of MMA-based specimen at the same instant shows the crack initiation in the adhesive material (see Fig. 8(c)). At the displacement of 4 mm, considerable AE activities start and besides the low-frequency AE signals, some other AE events with a frequency up to 250 kHz are captured. The last AE events' group with a frequency range of [300-400 kHz] initiates at the displacement of ~4.5 mm. All these AE activities continue to the displacement of 11 mm, where the final fracture occurs (see Fig. 8(d)). Using the camera images, captured during the test, the damage is started by crack nucleation in the adhesive layer at the notch tip which is then followed by adhesive failure at the steel/adhesive interface in the vicinity of the notch and at the lower edge of the specimen. Towards the end of the test, these two adhesive failures are connected.

In the case of the Epoxy-based specimens, the first AE activity occurs at the displacement of 0.6 mm which corresponds to the crack initiation at the adhesive material (see Fig. 9(c)). From this point to just before the final fracture of the specimen, limited number of AE events are recorded indicating that there is no considerable damage in the specimen, and that all the applied work on the specimen is stored in the form of strain energy. At the moment of the final fracture, some AE events with different frequency ranges, i.e. [100-200 kHz] and [400-500 kHz], are captured representing different damage mechanisms activated in the specimen at the same time (see Fig. 9(d)). Using the camera images, captured during the test, the damage starts first by crack initiation at the adhesive layer around the notch and then it propagates rapidly within the adhesive layer. At the final fracture, a complete adhesive failure at the steel/adhesive interface happens at one side of the specimen. While on the other side, delamination and fiber breakage at the CFRP skin are observed.

In order to investigate the evolution behavior of each damage mechanism by AE, it is essential to first distinguish and classify the different damage mechanisms according to their AE features. To achieve that, standard tests on the individual constituents are conducted to simulate and capture the AE signatures associated with the damage mechanisms that occur in the DLJ specimens. The specifications of the individual constituent tests are summarized in Table 2. All the tests are done according to the corresponding ASTM standard and the AE activities are captured by the AE sensor mounted on the specimens' surface.

The tensile and shear tests of the steel are shown in Figs. 10 and 11. The DIC strain distribution also confirms that the dominant stress components for the tensile and shear tests are normal and in-plane shear stresses respectively. The load-displacement curve and also the peak frequency distribution of the AE events recorded during these tests are shown in

Fig. 12. These AE signals correspond to the elastic and plastic deformation of the steel under tension and shear loading conditions. The AE events observed in the initial elastic deformation stage are due to the nucleation of a few dislocations at the grain boundary and also local yielding around inclusions, while the AE events in the plastic deformation stage are almost originated from dislocations interlocking, creating of new dislocation, stress concentration and extension of Luders bands in the steel [36]. As can be seen, regardless of the loading condition, there are three groups of AE signals in both specimens consisting of [100-200 kHz], [300-400 kHz], and [400-600 kHz]. In addition, comparing other AE features like amplitude, duration, rise time, counts, extra, showed that there is no considerable difference between the AE features of the shear and tensile tests. This fact shows that the originated AE signals due to steel deformation are mostly material-dependent not loading conditions-dependent. Therefore, all the AE signals collected from both tensile and shear tests are labelled as "Steel deformation" signals.

In order to capture the AE signals of plastic deformation and also crack growth under tensile and shear stresses in the adhesive material, the standard tensile, fracture mode I and mode II tests were conducted. To ensure pure mode I and mode II loads on the specimens, the modified Arcan test apparatus [33] was used. The geometry and dimensions of the coupons and also the tests apparatus are shown in Figs. 13-15. Only the results of MMA-based adhesive are presented here as an example. The DIC strain distribution again confirms that the dominant stress component for the tensile and mode I specimen is normal stress while the dominant stress component for mode II specimen is in-plane shear stress concentrated at the crack tip. The load-displacement curves and the frequency distribution of the AE signals recorded during the tensile, modes I and mode II loading of the adhesive specimens are

depicted in Fig. 16. It is clear that, regardless of the loading conditions and also the specimens' geometry, the recorded AE signals for the three different tests are similar in the sense that two classes of AE signals with the frequency of [100-200 kHz] and [300-350 kHz] are captured. Therefore, all the AE signals collected from these tests are labelled as "cohesive failure" signals.

In order to obtain the AE signals of the CFRP skin damage, CFRP tensile specimens with the same layup of the skin were subjected to tensile loading (see Fig. 17) and the originated AE signals were recorded by the AE sensor mounted on the specimen surface. The Scanning Electron Microscopy (SEM) images of the broken CFRP tensile specimen and CFRP skin of DLJ specimen are shown in Fig. 18. As it is clear, the dominant damage mechanisms for both specimens are similar and they are fiber breakage and delamination and also some matrix cracks. The load-displacement and the peak frequency distribution of the recorded AE signals are illustrated in Fig. 19. There are some clusters of AE signals with different frequency contents that can be related to different damage mechanisms observed in the SEM images. According to literature [12, 37-39], the first cluster with the lowest frequency can be devoted to matrix cracking and the cluster with the highest frequency may be related to the fiber breakage. The cluster with the medium frequency is also associated with the delamination. Regardless the type of sub-damages, the AE signals collected during the tension of CFRP are labelled as "skin failure".

The AE signals for the adhesive failure at steel/adhesive and CFRP/adhesive interfaces were obtained by conducting some Double Cantilever Beam (DCB) tests on the steel/steel and CFRP/CFRP adhesively-bonded specimens. A pre-crack was made by

inserting a Teflon film layer between the strips during the bonding process. The DCB test apparatus and the load-displacement curves are shown in Fig. 20. The signals of DCB tests are labelled as ”adhesive failure”. The images from the damaged surface of steel/steel and CFRP/CFRP DCB specimens are shown in Fig. 21. As it is clear, there is not any adhesive material on the steel surface which shows a complete “adhesive failure”. In the case of CFRP, although some small adhesive materials remained on the CFRP part, it is obviously seen that the dominant damage mechanism is still “adhesive failure” not “cohesive failure”.

The AE signals of individual constituents failure are collected from the aforementioned tests, and they are used to train an ensemble decision tree classifier. Thus, eight commonly used AE parameters consisting of amplitude, rise time, duration, counts, energy, RMS, centroid frequency, and peak frequency are extracted for each AE signal and fed into the classifier as the data features, and the signal label is defined as the response. This parameters are selected such that they have the lowest dependency on each other. The specifications of the training data is represented in Table 3.

Ensemble decision tree classifier refers to a hyper-parameter problem. To obtain the best parameters to create the ensemble model, the hyper-parameter optimization was done using a Bayesian optimization process with the maximum of 30 iterations. Three parameters consisting of number of learning cycles, learning rate and minimum leaf size and also three combination techniques consisting of Random Under-sampling Boosting, Adaptive Boosting, and Bootstrap aggregation (Bagging) were chosen for the optimization process. Based on the minimum objective value and the runtime of the model, Bayesian optimization method finally represented the optimized parameters as follows: combination technique:

bagging, number of learning cycles: 77, and the minimum leaf size: 1 (notice: learning rate is not defined for bagging technique).

Cross-Validation method was used to protect the classification against overfitting by partitioning the data set into 5 folds and estimating the accuracy on each fold. To this aim, first, all the data points (209638) are randomly divided into 5 groups. Then, 4 groups are selected for the training of the model. If the ensemble model contains *n* trees, these four groups are then divided into *n* subgroups. Then, each tree is trained by one of these *n* subgroups. When all the trees are trained sufficiently, the only remained group, among 5 initial groups, is used for the validation of the trained model. This process is repeated for four more times such that each of the other four groups is used as the validation dataset. The performance of the classifier is evaluated by the confusion matrix shown in Fig. 22. The overall accuracy of the classification for MMA-based and Epoxy-based training data set is 99.5 % and 99.8% respectively. This indicates that the classifier has been trained effectively and ensures its good performance to classify the DLJ specimen's signals. The largest error is associated with the "Steel deformation" in MMA-based specimen (25%).

After training the classifier, the AE signals of DLJ specimens are classified and labelled by the trained model. The total cumulative AE energy and cumulative AE energy curve of four aforementioned damage mechanisms for DLJ specimens is shown in Fig. 23. In the case of MMA-based specimen, damage is characterized by a progressive nature and it initiates at load levels which are much less than the maximum load. The AE accumulative curve (Fig. 23(a)) suggests that the dominant damage mechanism is cohesive failure which is consistent with the visually inspected results (see Fig. 7(a)). Adhesive failure AE signals represents the second highest class of damage featuring the steel/adhesive interfacial failure

at the lower edges of the specimen as depicted in Fig. 24. As some steel deformation signals are also captured, it is important to understand whether they are due to elastic or plastic deformation. Thus, the longitudinal strain (see Fig. 25) obtained by the DIC at the maximum load for the steel core (~0.002) is compared with the yield strain of the steel. This ensures that the captured signals are due to the elastic deformation of steel and there is no concern about any yielding of the steel core. Although the AE accumulative curve suggests that there is skin failure in the MMA-based specimen, visual inspection (see Fig. 7(a)) does not show any visible delamination or fiber breakage in the CFRP skin. Thus, this can be due to matrix cracking occurring locally at the crack tip singularity in the middle of the specimen's length. To verify this hypothesis, the strain captured by the FOS, at the maximum load, is analyzed (see Fig. 26). It is clear from the strain distribution that the maximum strain is much less than the failure strain of the CFRP skin (~0.006 as opposed to ~0.020). However, according to Fig. 19, AE events with the frequency less than 150 kHz can be seen at this strain level which could be related to matrix cracking that usually has the minimum frequency compared with delamination and fiber breakage [37, 38]. The strain distribution shows that the strain is minimum at the both edges of the specimen and it gradually increases when moving to the middle of the specimen where the notch is. Due to adhesive failure at the steel/adhesive interface at the lower edge of the specimen, the CFRP skin experiences compression due to bending. This is reflected by the negative strain values in Fig. 26.

Unlike the MMA-based specimen, the damage in the Epoxy-based specimen (see Fig. 23(b)) occurs instantaneously at the maximum load. In this case, the dominant damage mechanisms captured by AE are skin failure and adhesive failure. Despite the fact that the strain distribution captured by the FOS on the CFRP skin outer surface is similar to the

MMA-based specimen, the stress singularity due to the crack tip in the case of the Epoxy-based adhesive leads to local fiber breakage and delamination initiating from the inner surface (see Fig. 7(b)). This can be attributed to the brittle nature of the Epoxy-based adhesive as it does not undergo as much plastic deformation as the MMA-based counterpart. Consequently, this results in higher stress concentration at the crack tip leading to the CFRP skin failure. Again, the steel deformation signals are checked to ensure that they are due to the elastic deformation of the steel core with no sign of yielding.

6 Conclusion

The objective of the present work was damage characterization of the bi-material double-lap adhesively-bonded joints using Acoustic Emission (AE). Double-Lap Joint (DLJ) specimens were fabricated of a steel core bonded to two CFRP skins by two types of adhesive; a ductile "MMA-based" and a brittle "Epoxy-based". The specimens were then subjected to the tensile loading while AE was in-situ monitoring the damage in the joints. FOS and DIC systems were used to measure the strain on the specimens' surfaces. In order to distinguish and classify different damage mechanisms by AE, standard tests were conducted on the individual constituents. The AE signals captured during these tests were used to train an ensemble bagged tree classifier. The best parameters of the ensemble model were obtained by Bayesian optimization, and the confusion matrix showed that the model was sufficiently trained with the accuracy of 99.5% and 99.8% for Methacrylate-based and Epoxy-based specimens respectively. Afterwards, the trained model was used to classify the AE signals of the double-lap specimens. The AE demonstrated that the dominant damage mechanisms in the case of the Methacrylate-based were cohesive and adhesive failures while in the case of the Epoxy-based they were CFRP skin failure and adhesive failure. These

dominant damage mechanisms captured by AE were consistent with the DIC, FOS and camera results. This study showed the potential of AE technique for damage characterization of adhesively-bonded bi-material joints.

Acknowledgments

This research was carried out within the project "QUALIFY–Enabling Qualification of Hybrid Joints for Lightweight and Safe Maritime Transport", co-funded by the INTERREG 2SeasMers Zeeën programme.

References

[1] Sousa JM, Correia JR, Firmo JP, Cabral-Fonseca S, Gonilha J. Effects of thermal cycles on adhesively bonded joints between pultruded GFRP adherends. Compos Struct 2018, 202, 518-529.

[2] Mariam M, Afendi M, Abdul Majid MS, Ridzuan MJM, Azmi AI, Sultan MTH. Influence of hydrothermal ageing on the mechanical properties of an adhesively bonded joint with different adherends. Composites Part B 2019, 165; 572-585.

[3] Mu W, Qin G, Na J, Tan W, Liu H, Luan J. Effect of alternating load on the residual strength of environmentally aged adhesively bonded CFRP-aluminum alloy joints. Composites Part B 2019, 168; 87-97.

[4] Yu QQ, Gu XL, Zhao XL, Zhang D, Huang H, Jiang C. Characterization of model uncertainty of adhesively bonded CFRP-to-steel joints. Compos Struct 2019, 215; 150-165.

[5] Heshmati M, Haghani R, Al-Emrani M. Durability of bonded FRP-to-steel joints: Effects of moisture, de-icing salt solution, temperature and FRP type. Composites Part B 2017, 119; 153-167.

[6] Heshmati M, Haghani R, Al-Emrani M, André A. On the strength prediction of adhesively bonded FRP-steel joints using cohesive zone modelling. Theor Appl Fract Mech 2018, 93: 64–78.

[7] Heshmati M, Haghani R, Al-Emrani M. Durability of CFRP/steel joints under cyclic wet-dry and freeze-thaw conditions. Composites Part B 2017, 126; 211-226.

[8] Heshmati M, Haghani R, Al-Emrani M. Environmental durability of adhesively bonded FRP/steel joints in civil engineering applications: State of the art. Composites Part B 2015, 81; 259-275.

[9] Heshmati M, Haghani R, Al-Emrani M. Effects of moisture on the long-term performance of adhesively bonded FRP/steel joints used in bridges. Composites Part B 2016, 92; 447-462.

[10] Romhány G, Czigány T, Karger-Kocsis J. Failure assessment and evaluation of damage development and crack growth in polymer composites via localization of acoustic emission events: A Review. Polym Rev 2017, 57(3); 397-439.

[11] De Rosa IM, Santulli C, Sarasini F. Acoustic emission for monitoring the mechanical behaviour of natural fibre composites: A literature review. Composites Part A 2009, 40(9); 1456-1469.

[12] Saeedifar M, Ahmadi Najafabadi M, Zarouchas D, Hosseini Toudeshky H, Jalalvand M. Clustering of interlaminar and intralaminar damages in laminated composites under indentation loading using acoustic emission. Composites Part B 2018, 144; 206-219.

[13] Lee YH, Lim DW, Choi JH, Kweon JH, Yoon MK. Failure load evaluation and prediction of hybrid composite double-lap joints. Compos Struct 2010, 92; 2916–2926.

[14] Fotouhi M, Saeedifar M, Sadeghi S, Ahmadi Najafabadi M, Minak G. Investigation of the damage mechanisms for mode I delamination growth in foam core sandwich composites using acoustic emission. Struct Health Monit 2015, 14(3); 265–280.

[15] Xu D, Liu PF, Li JG, Chen ZP. Damage mode identification of adhesive composite joints under hygrothermal environment using acoustic emission and machine learning. Compos Struct 2019, 211; 351–363.

[16] Kupski J, Teixeira de Freitas S, Zarouchas D, Camanho PP, Benedictus R. Composite layup effect on the failure mechanism of single lap bonded joints. Compos Struct 2019, 217; 14–26.

[17] Zhang Y, Ma Y. Application of supervised machine learning algorithms in the classification of sagittal gait patterns of cerebral palsy children with spastic diplegia. Comput Biol Med 2019, 106; 33-39.

[18] Gan H, Huang R, Luo Z, Xi X, Gao Y. On using supervised clustering analysis to improve classification performance. Inf Sci 2018; 454–455: 216–28.

[19] ASTM D3528-96. Standard test method for strength properties of double-lap shear adhesive joints by tension loading. West Conshohocken, PA, ASTM International; 2016.

[20] Barile C, Casavola C, Pappalettera G, Vimalathithan PK. Characterization of adhesive bonded CFRP laminates using full-field digital image stereo-correlation and finite element analysis. Compos Sci Technol 2019; 169: 16-25.

[21] Finkel P, Mitchell JR, Carlos MF. Experimental study of "Auto Sensor Test-Self Test Mode" for acoustic emission system performance verification. AIP Conference Proceedings 509, 1995 (2000); https://doi.org/10.1063/1.1291316.

[22] Barile C, Casavola C, Pappalettera G, Vimalathithan PK. Experimental Wavelet Analysis of Acoustic Emission Signal Propagation in CFRP. Eng Fract Mech 2019; 210: 400-7.

[23] Barile C. Innovative mechanical characterization of CFRP by using acoustic emission technique. Eng Fract Mech 2019; 210: 414-21.

[24] ASTM E976–10. Standard guide for determining the reproducibility of acoustic emission sensor response. West Conshohocken, PA, ASTM International; 2010.

[25] Eick CF, Zeidat N, Zhao Z. Supervised Clustering – Algorithms and Benefits. Proceedings of the 16th IEEE International Conference on Tools with Artificial Intelligence (ICTAI 2004), 2004.

[26] Ismaili OA, Lemaire V, Cornuéjols A. Supervised Pre-processings Are Useful for Supervised Clustering. In: Wilhelm A, Kestler H (eds). Analysis of Large and Complex Data. Studies in Classification, Data Analysis, and Knowledge Organization. Springer, Cham, 2016.

[27] Pliakos K, Vens C. Mining features for biomedical data using clustering tree ensembles. J Biomed Inf 2018, 85; 40-48.

[28] Breiman L, Friedman JH, Olshen RA, Stone CJ. Classification and regression trees. Chapman & Hall 1984, ISBN 978-0-412-04841-8.

[29] Breiman L. Bagging Predictors. Mach Learn 1996, 26; 123–140.

[30] ASTM E8/E8M-16a. Standard test methods for tension testing of metallic materials. West Conshohocken, PA, ASTM International; 2016.

[31] ASTM B831-14. Standard Test Method for Shear Testing of Thin Aluminum Alloy Products. West Conshohocken, PA, ASTM International; 2014.

[32] ASTM D638-14. Standard Test Method for Tensile Properties of Plastics. West Conshohocken, PA, ASTM International; 2014.

[33] Hasanpour R, Choupani N. Rock fracture characterization using the modified Arcan test specimen. Int J Rock Mech Min Sci 2009, 46(2); 346-354.

[34] ASTM D5528-13. Standard test method for mode I interlaminar fracture toughness of unidirectional fiber-reinforced polymer matrix composites. West Conshohocken, PA, ASTM International; 2013.

[35] ASTM D3039 / D3039M-17. Standard test method for tensile properties of polymer matrix composite materials. West Conshohocken, PA, ASTM International; 2017.

[36] Akbari M, Ahmadi M. The application of acoustic emission technique to plastic deformation of low carbon steel. Physics Procedia 2010, 3(1); 795-801

[37] Saeedifar M, Ahmadi Najafabadi M, Zarouchas D, Hosseini Toudeshky H, Jalalvand M. Barely visible impact damage assessment in laminated composites using acoustic emission. Composites Part B 2018, 152; 180-192.

[38] De Groot PJ, Wijnen PAM, Janssen RBF. Real-time frequency determination of acoustic emission for different fracture mechanisms in carbon/epoxy composites. Compos Sci Technol 1995, 55; 405–412.

[39] Gutkin R, Green CJ, Vangrattanachai S, et al. On acoustic emission for failure investigation in CFRP: pattern recognition and peak frequency analyses. Mech Syst Signal Process 2011; 25: 1393–407.

List of Figure captions

Fig. 1. The general test pyramid.

Fig. 2. The flowchart of the damage characterization process.

Fig. 3. Schematic of the DLJ specimen (dimensions in mm).

Fig. 4. The DLJ test apparatus.

Fig. 5. The FOS path on the CFRP skin.

Fig. 6. The load-displacement curve of a) MMA-based, and b) Epoxy-based specimens.

Fig. 7. Different damage mechanisms in the fractured specimens a) MMA-based and b) Epoxy-based.

Fig. 8. a) The load and AE frequency versus the displacement, and the camera images from the MMA-based specimen at b) the beginning of loading, c) the moment of AE activities initiation, and d) the final fracture.

Fig. 9. a) The load and AE frequency versus the displacement, and the camera images from the Epoxy-based specimen at b) the beginning of loading, c) the moment of AE activities initiation, and d) the final fracture.

Fig. 10. The tensile tests of the steel.

Fig. 11. The shear tests of the steel.

Fig. 12. The load-displacement and peak frequency distribution of a) Tensile, and b) Shear tests of steel.

Fig. 13. The tensile tests of the adhesive material.

Fig. 14. The mode I tests of the adhesive material.

Fig. 15. The mode II tests of the adhesive material.

Fig. 16. The load-displacement curves of a) Tensile, b) Mode I, and c) Mode II tests of MMA-based adhesive.

Fig. 17. CFRP tensile test.

Fig. 18. The SEM images from the CFRP tensile specimen and CFRP skin of DLJ specimen.

Fig. 19. The load-displacement curve and the frequency distribution of the AE events of the CFRP tensile test.

Fig. 20. a) Schematic of DCB specimens, DCB test apparatus and load-displacement curves for b) CFRP/CFRP, and c) steel/steel adhesively-bonded specimens.

Fig. 21. The damaged surface of a) steel made and b) CFRP made DCB specimens.

Fig. 22. The confusion matrix of the trained model for training data set of specimens; a) MMA-based and b) Epoxy-based.

Fig. 23. The total cumulative AE energy and cumulative AE energy curve of different damage mechanisms for a) MMA-based, and b) Epoxy-based DLJ specimens.

Fig. 24. (a) and (b) Detected adhesive failure during the loading by DIC, and c) the progressed adhesive failure at the end of the test for MMA-based specimen.

Fig. 25. The longitudinal strain obtained by DIC at the maximum load for the steel core.

Fig. 26. Longitudinal strain distribution in the CFRP skin obtained by FOS (Segments 1 to 3 have been shown in Fig. 5)

List of Table captions

Table 1. Mechanical properties of the constituent materials.

Table 2. The specifications of the individual constituent tests.

Table 3. The specification of the training data for the ensemble decision tree classifier.

Full-scale structure

Components
and subcomponents

Structural details

Test coupons

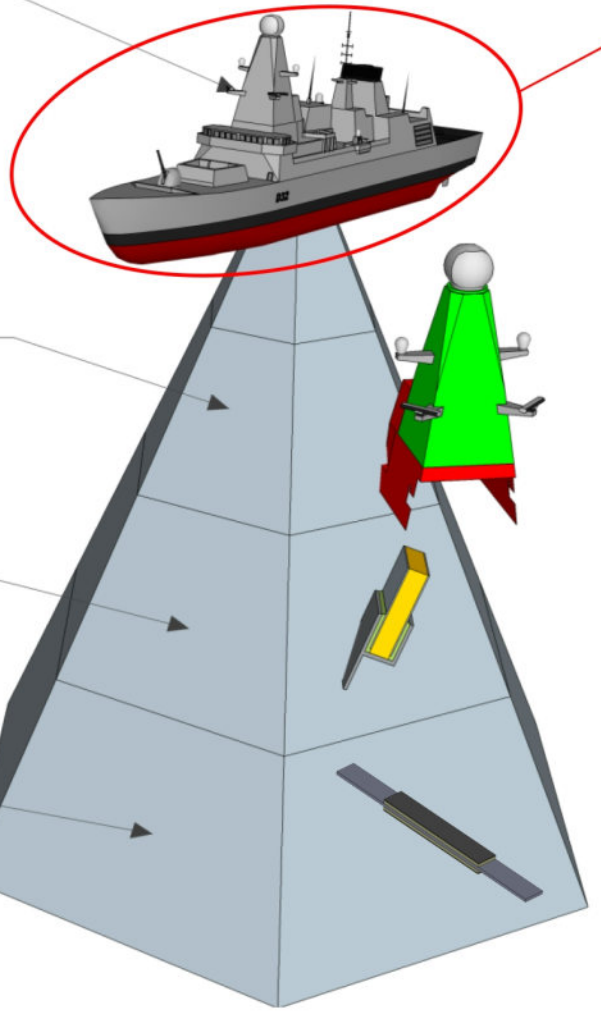

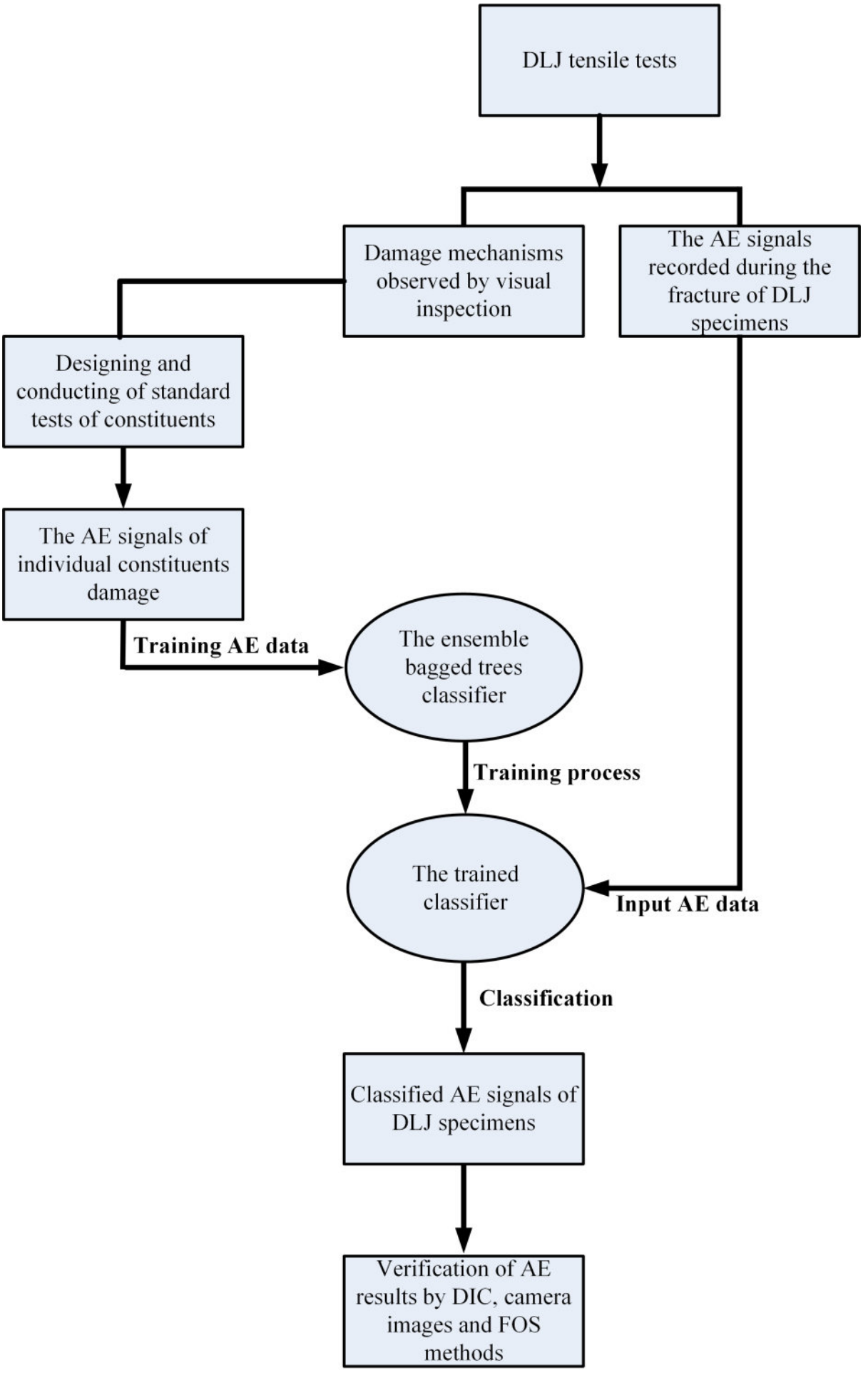
DLJ tensile tests
Damage mechanisms observed by visual inspection
The AE signals recorded during the fracture of DLJ specimens
Designing and conducting of standard tests of constituents
The AE signals of individual constituents damage
Training AE data
The ensemble bagged trees classifier
Training process
The trained classifier
Input AE data
Classification
Classified AE signals of DLJ specimens
Verification of AE results by DIC, camera images and FOS methods

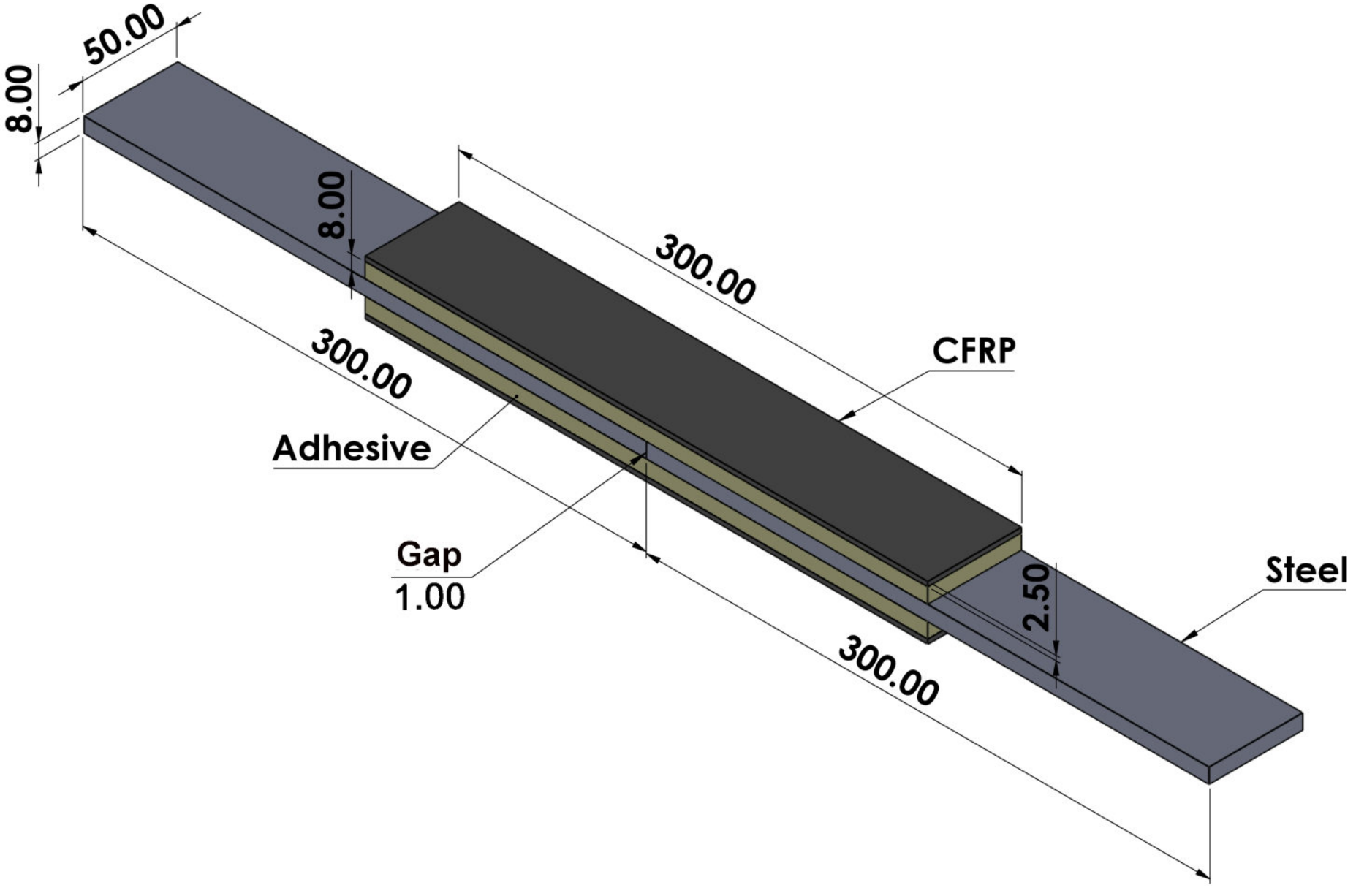
50.00
8.00
8.00
300.00
300.00
CFRP
Adhesive
Gap
1.00
Steel
2.50
300.00

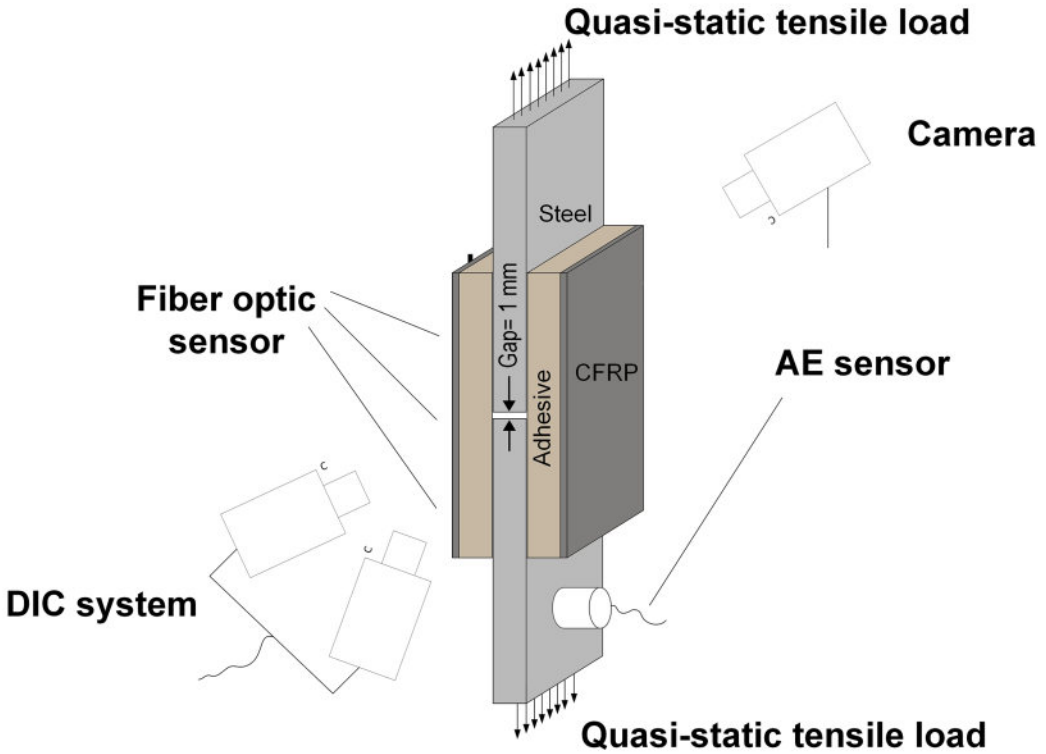
Quasi-static tensile load
Camera
Steel
Fiber optic sensor
Gap= 1 mm
CFRP
AE sensor
Adhesive
DIC system
Quasi-static tensile load

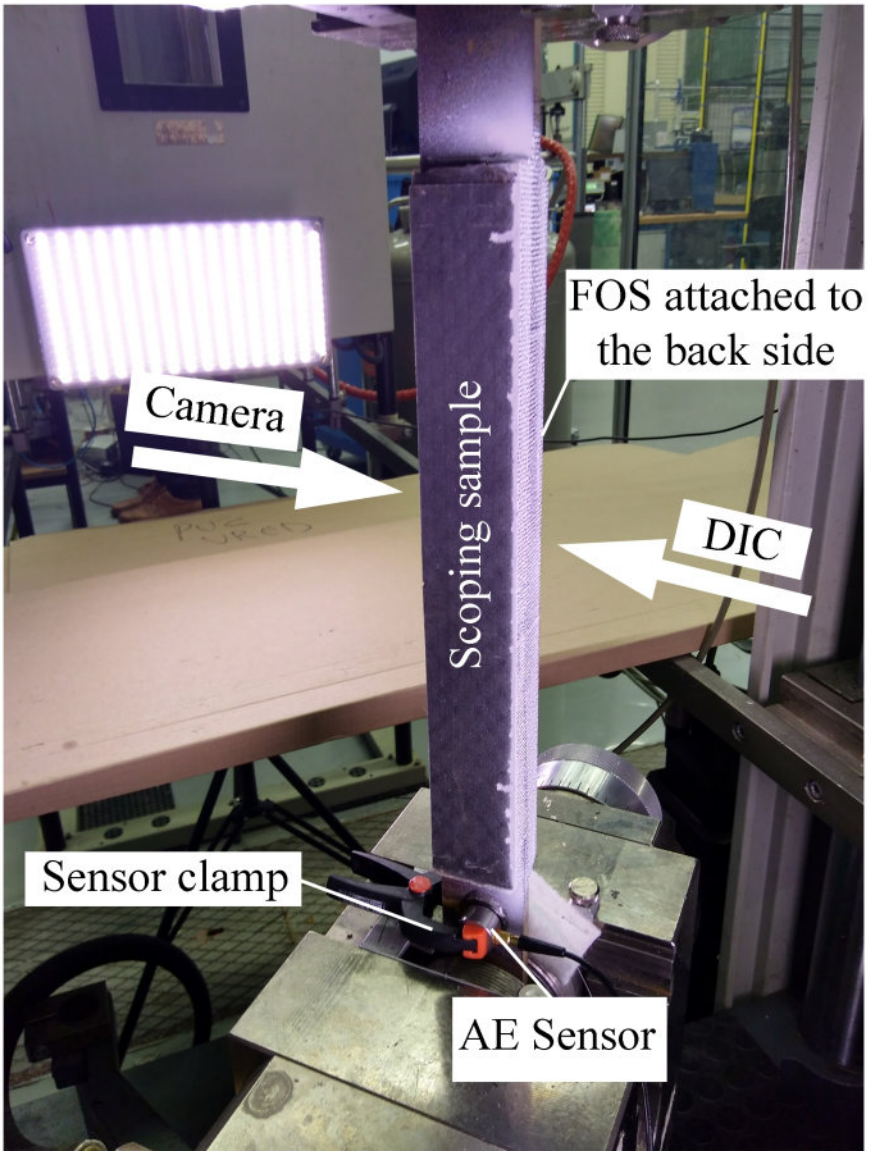
FOS attached to the back side
Camera
Scoping sample
DIC
Sensor clamp
AE Sensor

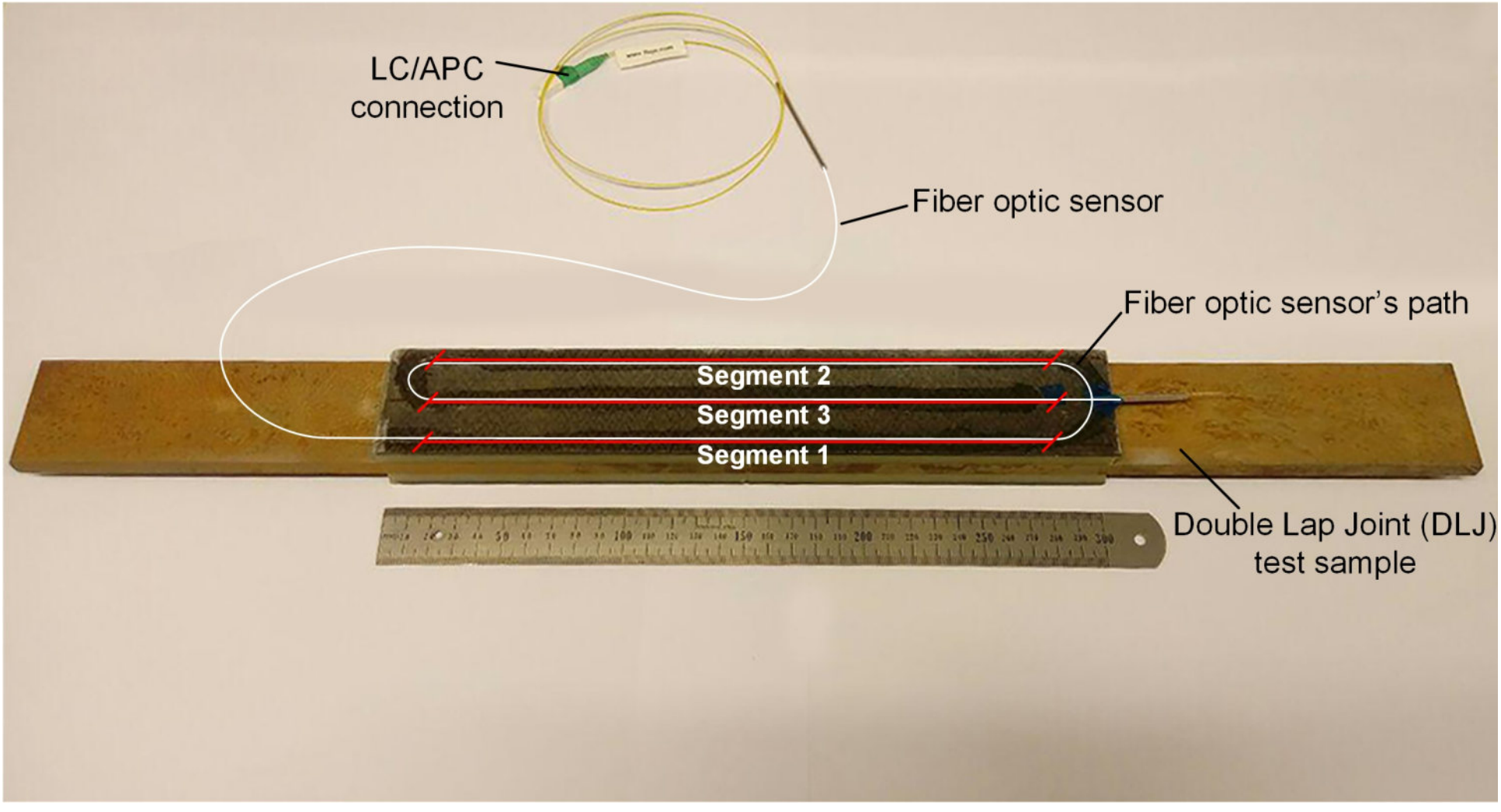
LC/APC
connection
Fiber optic sensor
Fiber optic sensor's path
Segment 2
Segment 3
Segment 1
Double Lap Joint (DLJ)
test sample

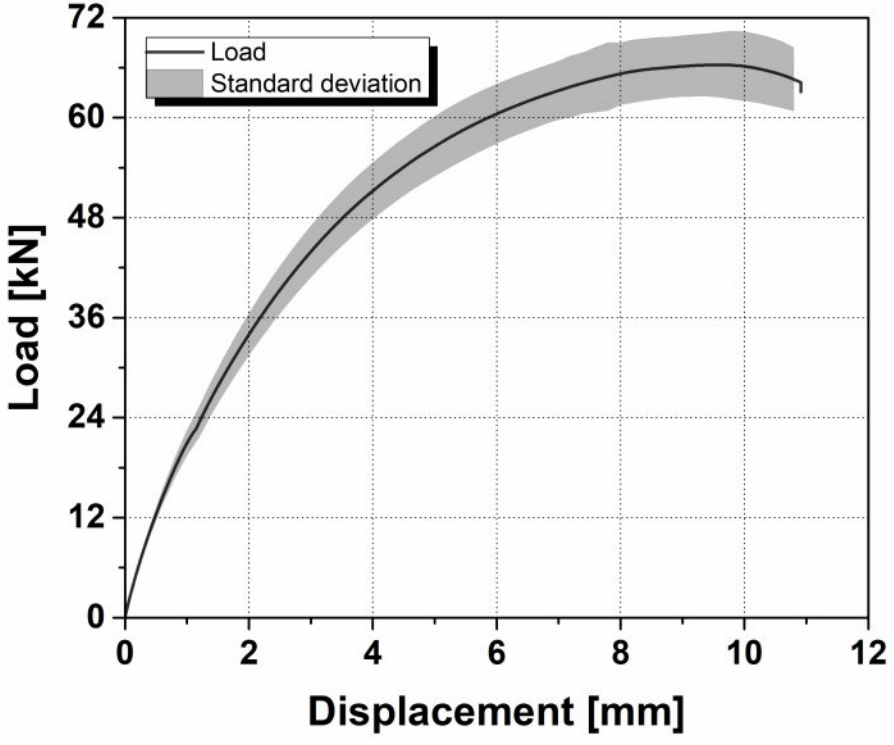
Load
Standard deviation
Load [kN]
Displacement [mm]
0
12
24
36
48
60
72
0
2
4
6
8
10
12

(a)

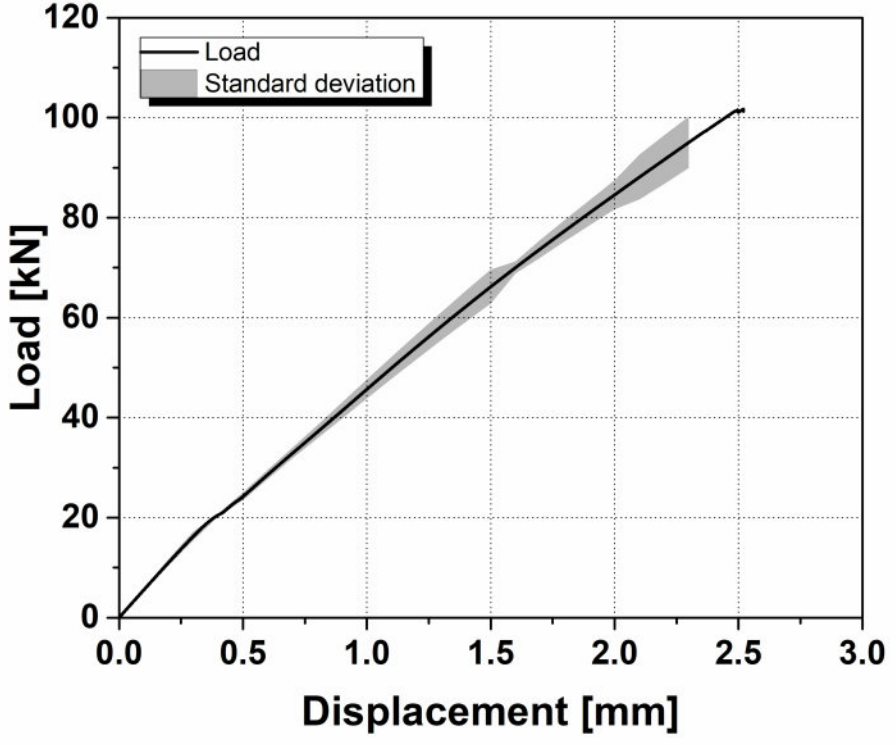
Load
Standard deviation
Load [kN]
Displacement [mm]
0
20
40
60
80
100
120
0.0
0.5
1.0
1.5
2.0
2.5
3.0

(b)

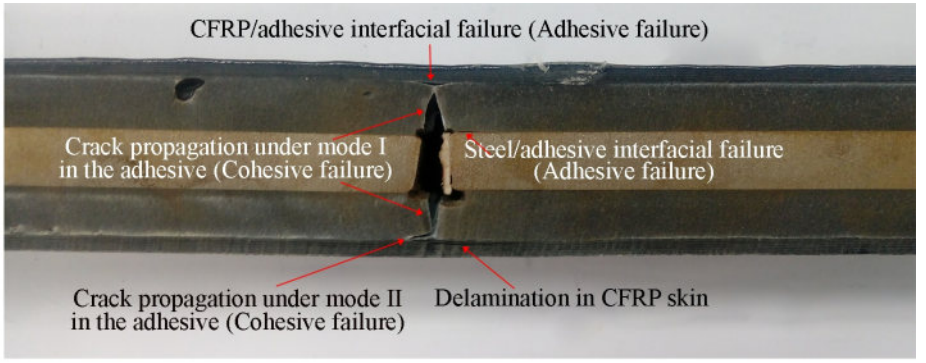
CFRP/adhesive interfacial failure (Adhesive failure)
Crack propagation under mode I
in the adhesive (Cohesive failure)
Steel/adhesive interfacial failure
(Adhesive failure)
Crack propagation under mode II
in the adhesive (Cohesive failure)
Delamination in CFRP skin

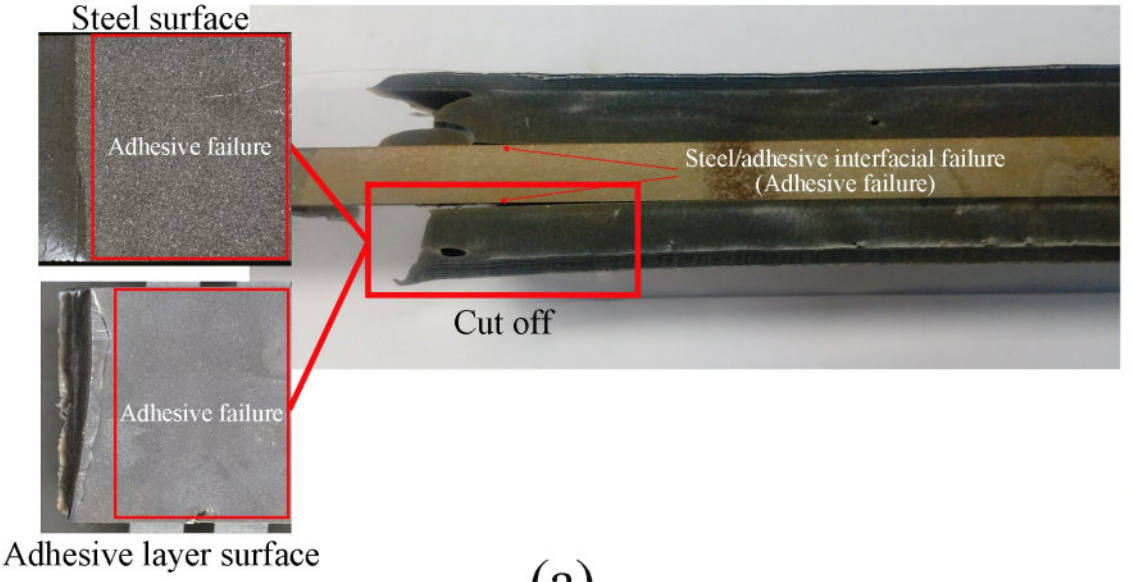
Steel surface
Adhesive failure
Steel/adhesive interfacial failure
(Adhesive failure)
Cut off
Adhesive failure
Adhesive layer surface

(a)

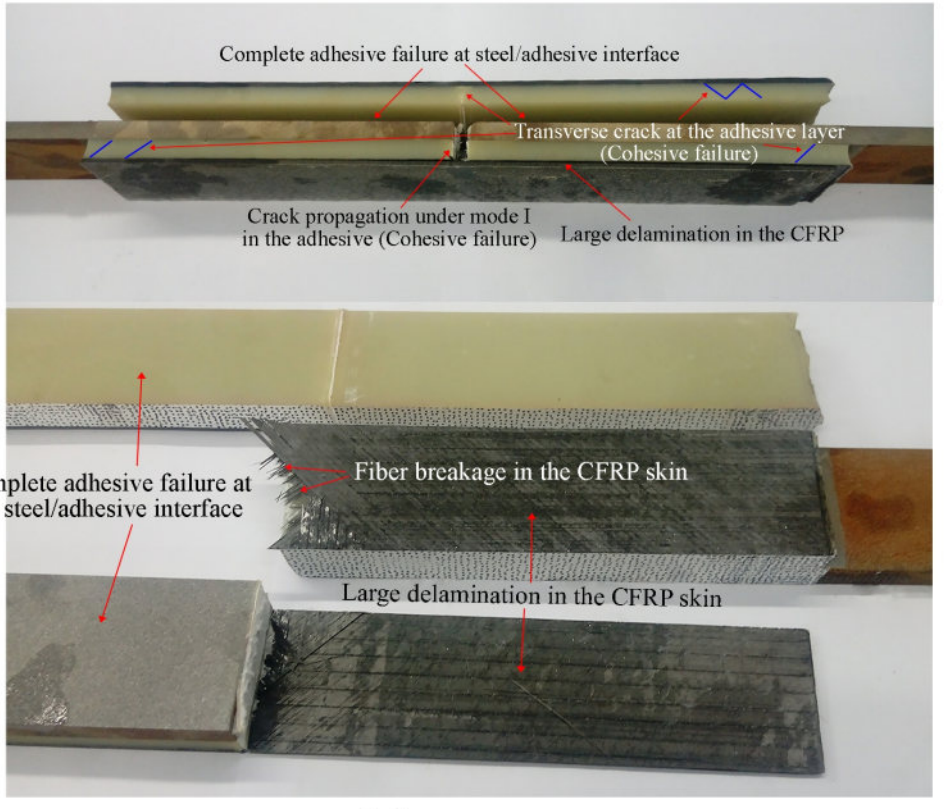
Complete adhesive failure at steel/adhesive interface
Transverse crack at the adhesive layer
(Cohesive failure)
Crack propagation under mode I
in the adhesive (Cohesive failure)
Large delamination in the CFRP
Complete adhesive failure at
the steel/adhesive interface
Fiber breakage in the CFRP skin
Large delamination in the CFRP skin

(b)

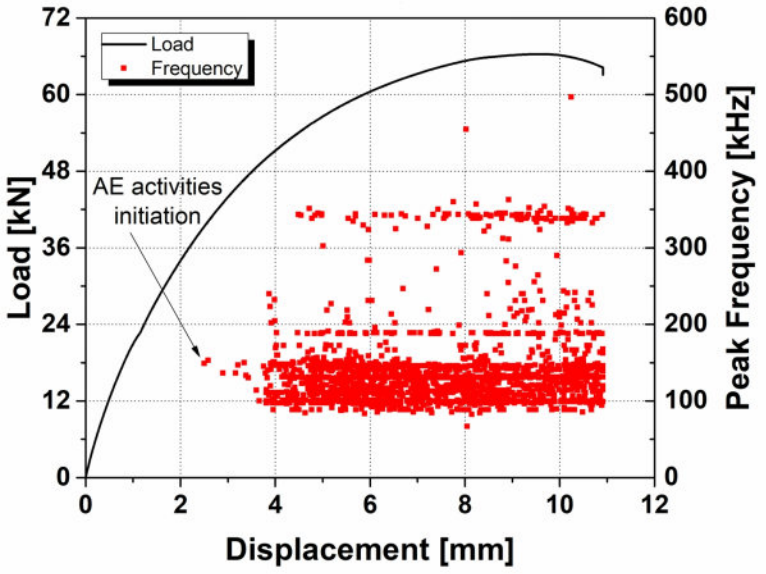
Load
Frequency
AE activities
initiation
Load [kN]
Peak Frequency [kHz]
Displacement [mm]
0
12
24
36
48
60
72
0
100
200
300
400
500
600
0
2
4
6
8
10
12

(a)

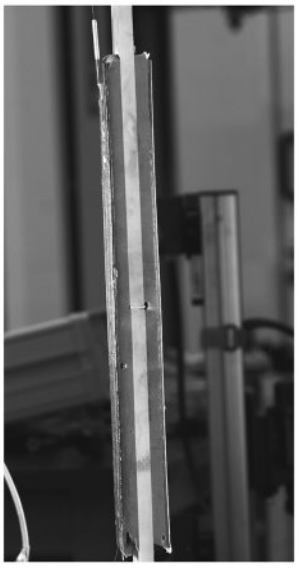

(b)

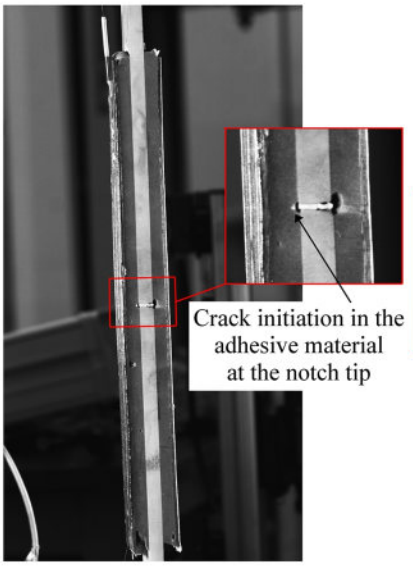
Crack initiation in the
adhesive material
at the notch tip

(c)

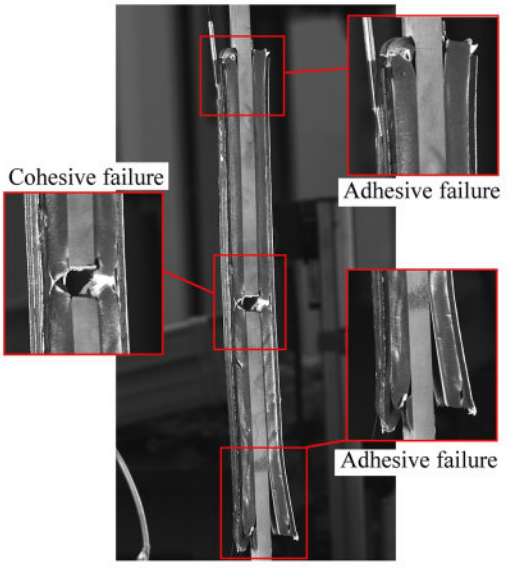
Cohesive failure
Adhesive failure
Adhesive failure

(d)

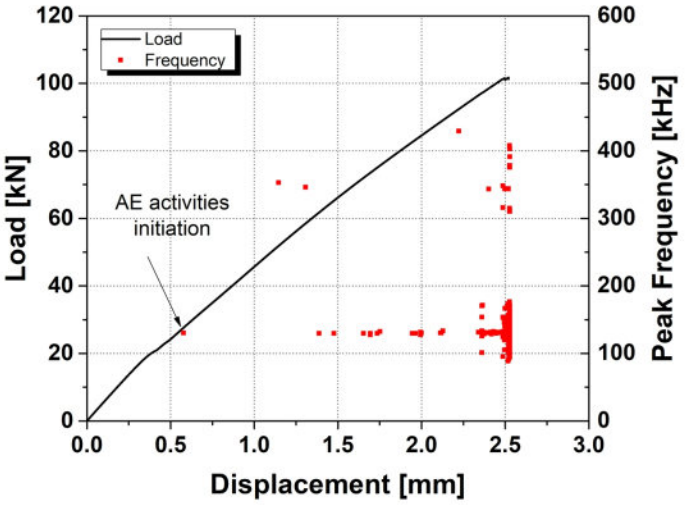
Load
Frequency
AE activities
initiation
Load [kN]
Peak Frequency [kHz]
Displacement [mm]
0
20
40
60
80
100
120
0
100
200
300
400
500
600
0.0
0.5
1.0
1.5
2.0
2.5
3.0

(a)

(b)

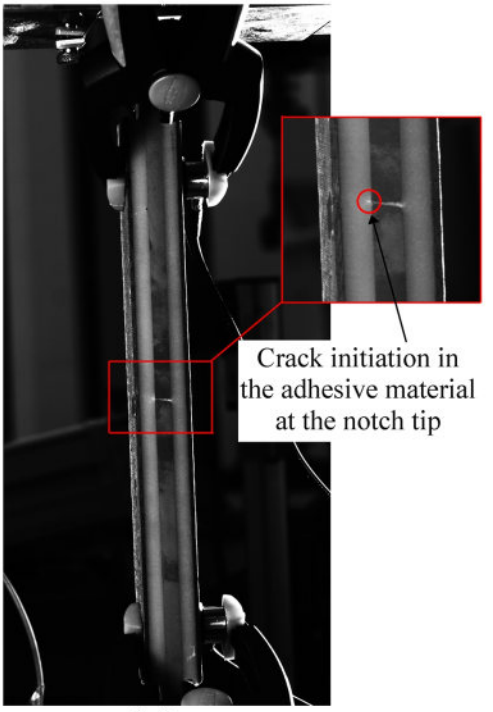
Crack initiation in
the adhesive material
at the notch tip

(c)

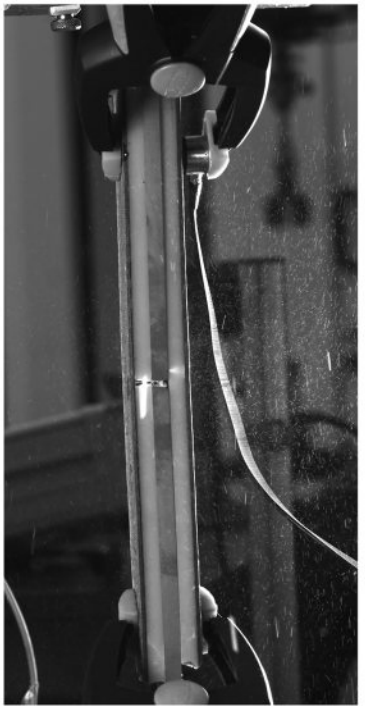

(d)

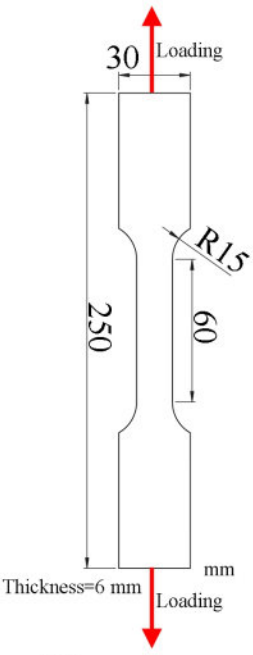

Drawing

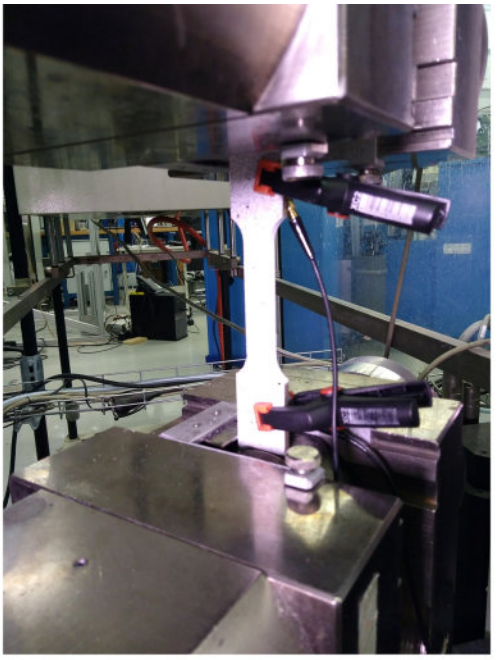

Before loading

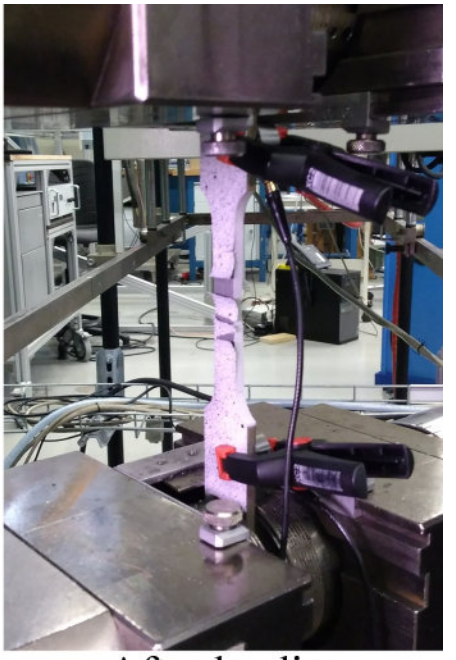

After loading

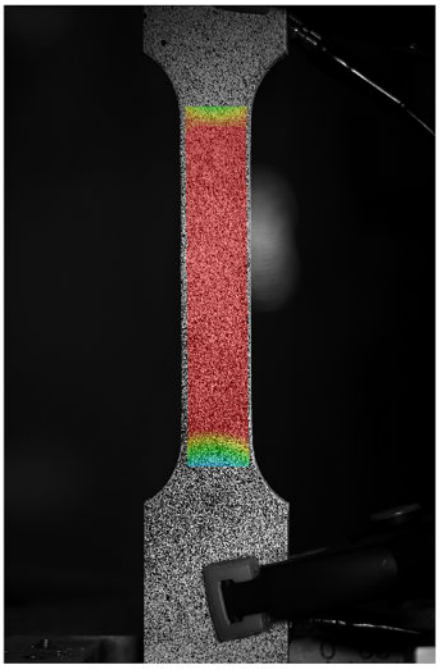

Longitudinal strain contour obtained by DIC

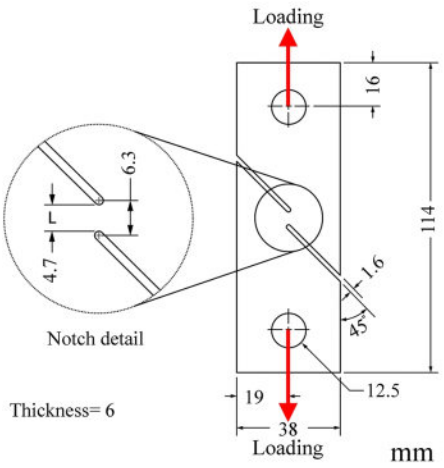

Drawing

Before loading

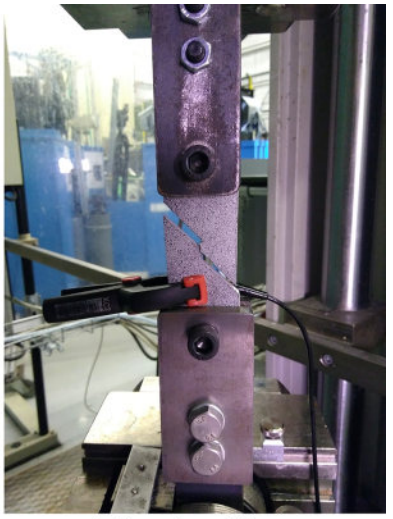

After loading

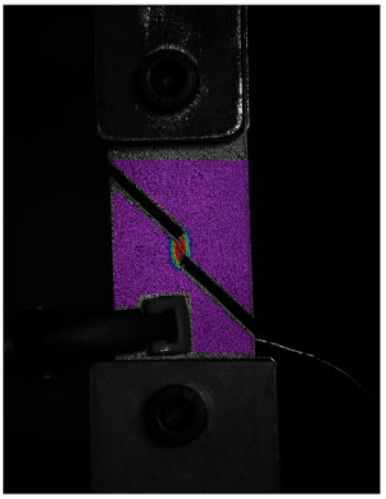

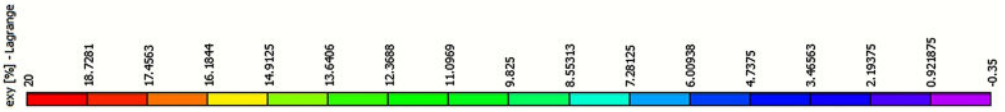

Shear strain contour obtained by DIC

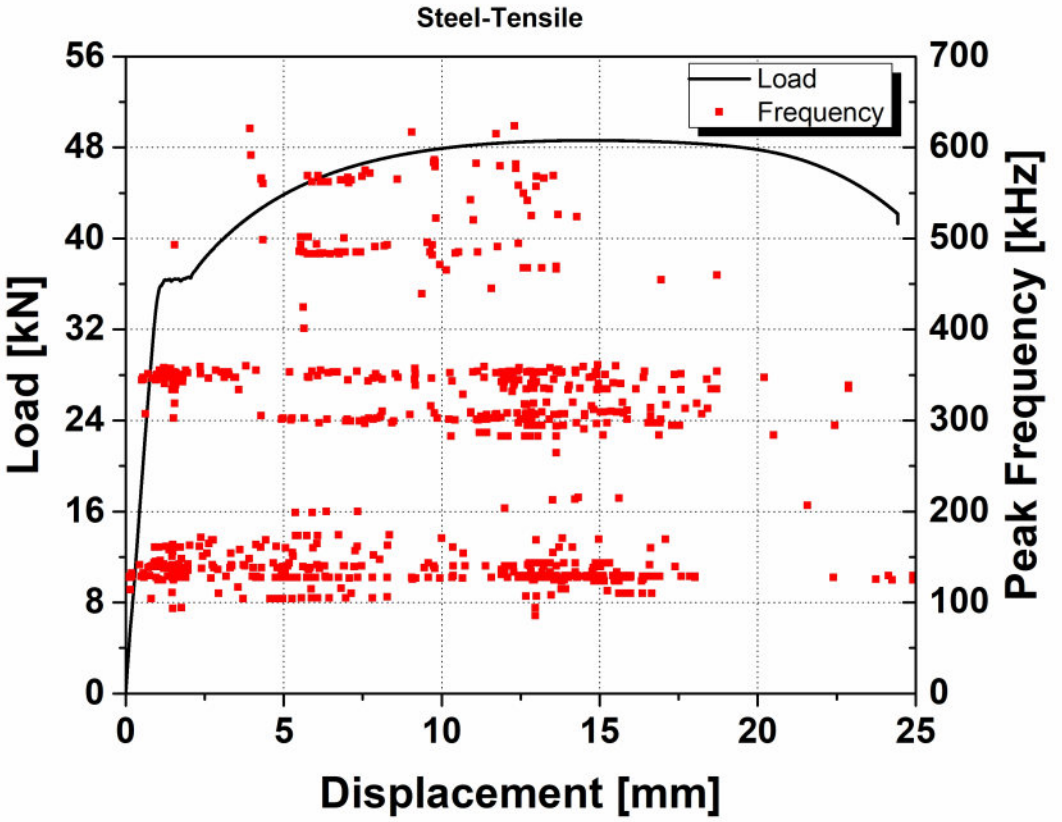
Steel-Tensile
Load
Frequency
Load [kN]
Peak Frequency [kHz]
Displacement [mm]
0
8
16
24
32
40
48
56
0
100
200
300
400
500
600
700
0
5
10
15
20
25

(a)

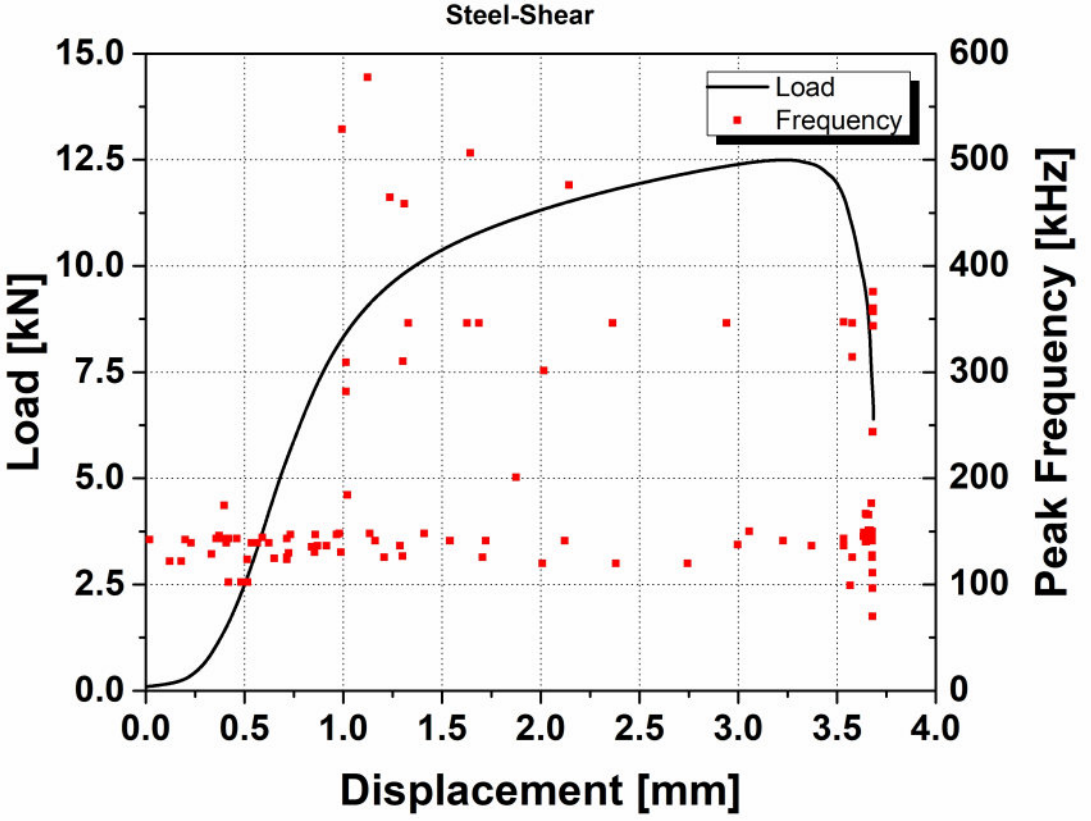
Steel-Shear
Load
Frequency
Load [kN]
Peak Frequency [kHz]
Displacement [mm]
0.0
2.5
5.0
7.5
10.0
12.5
15.0
0
100
200
300
400
500
600
0.0
0.5
1.0
1.5
2.0
2.5
3.0
3.5
4.0

(b)

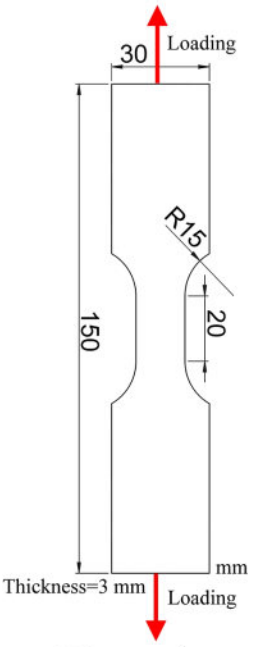

Drawing

Before loading

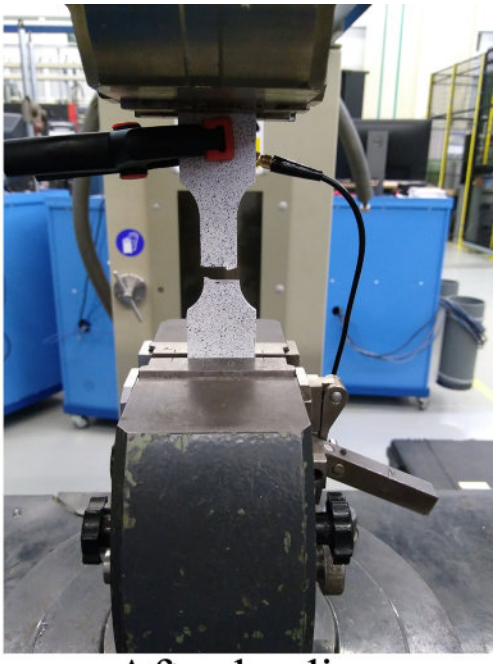

After loading

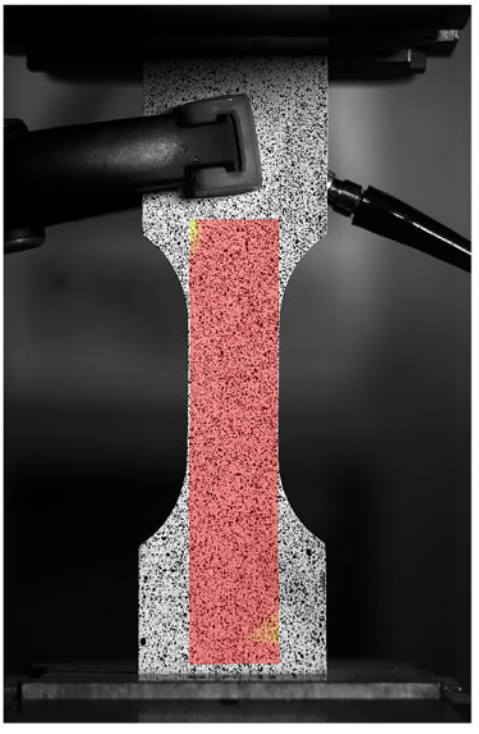

Longitudinal strain distribution obtained by DIC

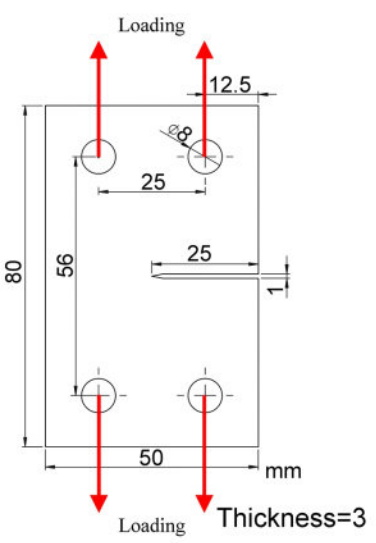

Drawing

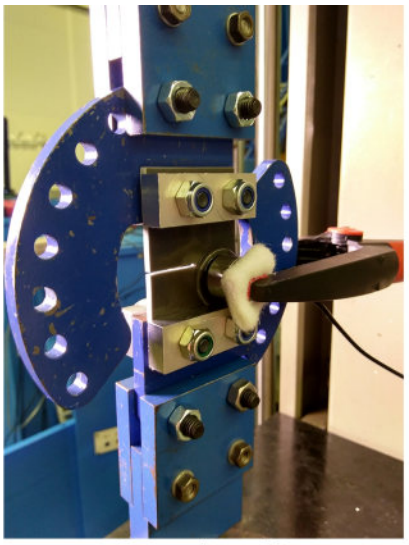

Before loading

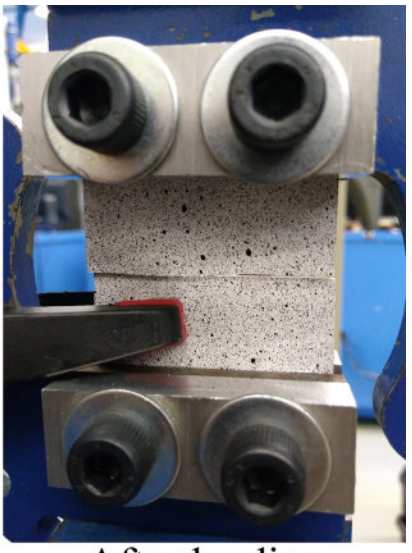

After loading

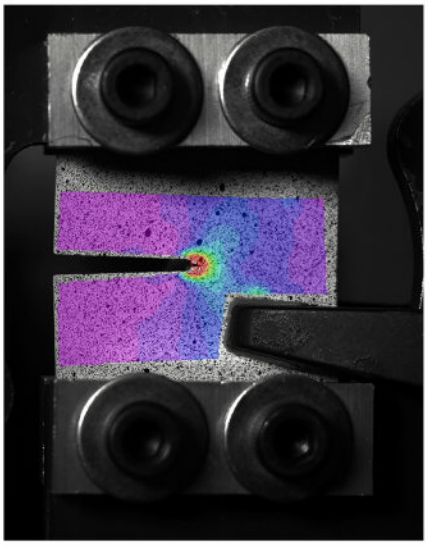

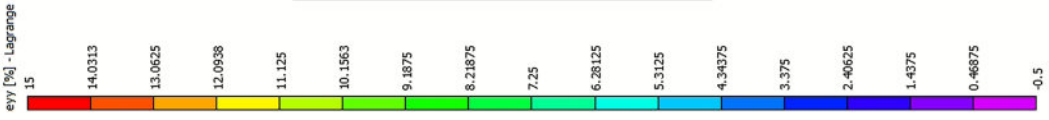

Normal strain distribution obtained by DIC

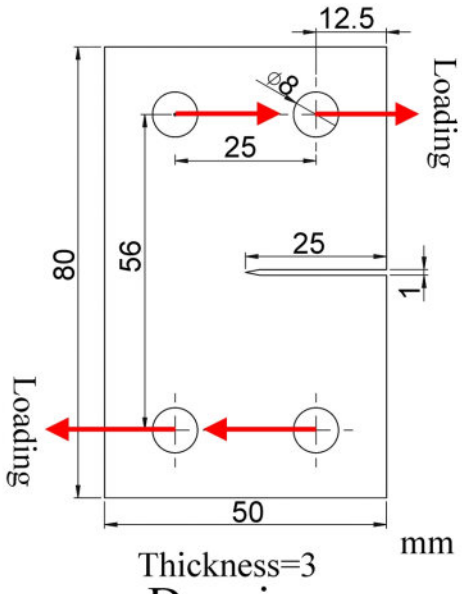

Drawing

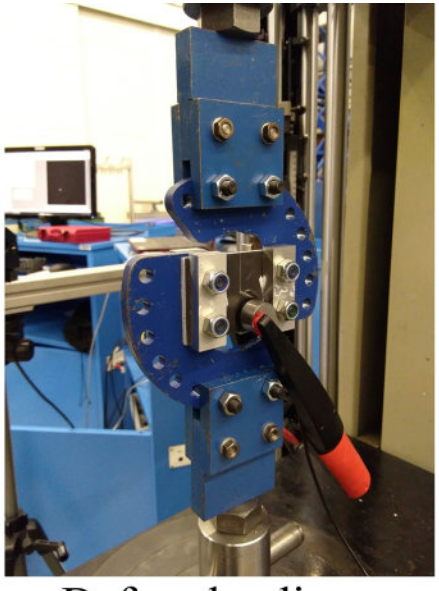

Before loading

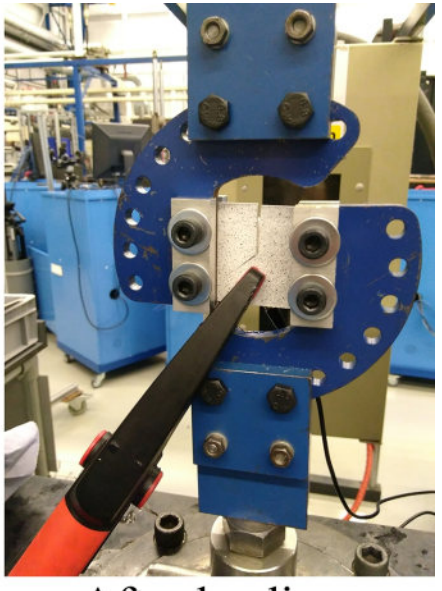

After loading

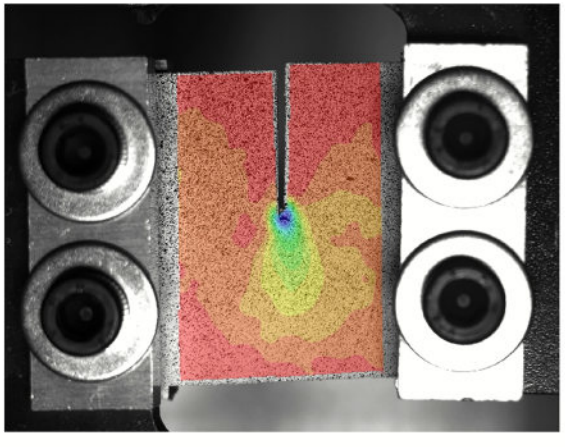

Shear strain distribution obtained by DIC

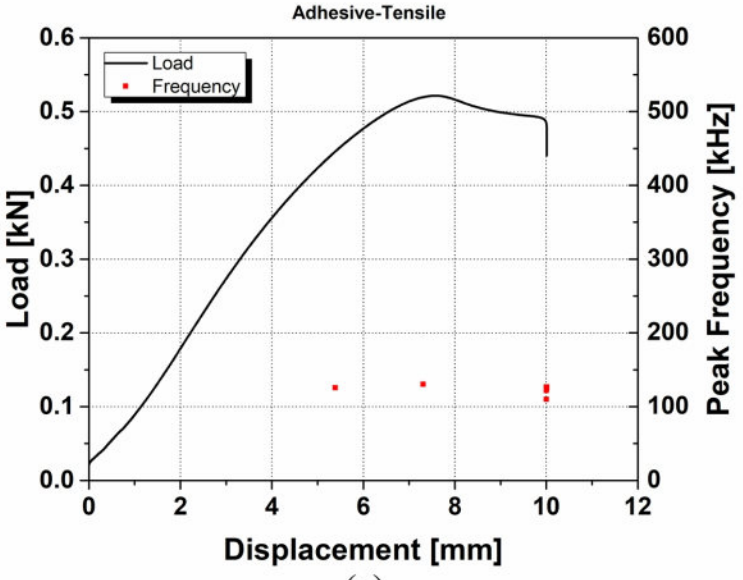
Adhesive-Tensile
Load
Frequency
Load [kN]
Peak Frequency [kHz]
Displacement [mm]
0.0
0.1
0.2
0.3
0.4
0.5
0.6
0
100
200
300
400
500
600
0
2
4
6
8
10
12

(a)

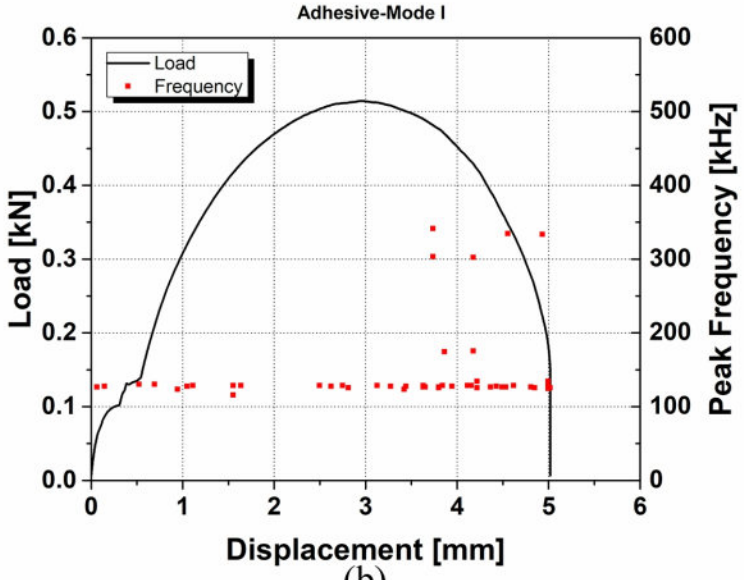
Adhesive-Mode I
Load
Frequency
Load [kN]
Peak Frequency [kHz]
Displacement [mm]
0.0
0.1
0.2
0.3
0.4
0.5
0.6
0
100
200
300
400
500
600
0
1
2
3
4
5
6

(b)

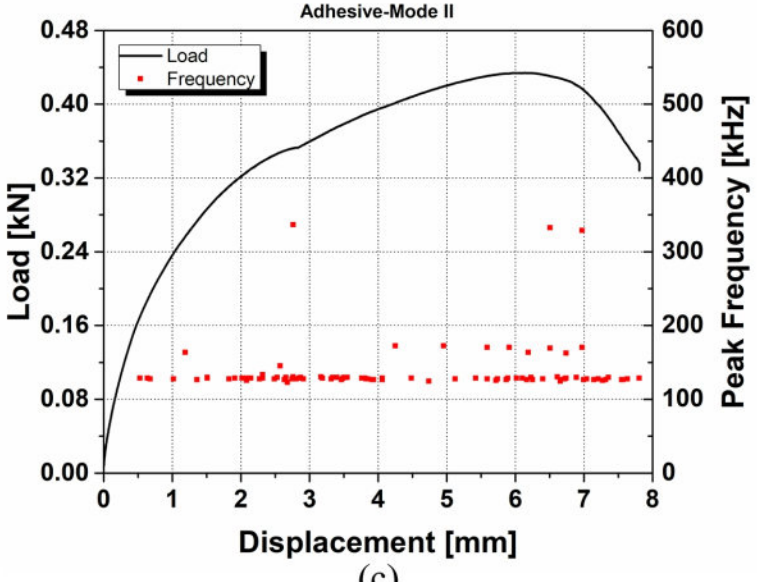
Adhesive-Mode II
Load
Frequency
Load [kN]
Peak Frequency [kHz]
Displacement [mm]
0.00
0.08
0.16
0.24
0.32
0.40
0.48
0
100
200
300
400
500
600
0
1
2
3
4
5
6
7
8

(c)

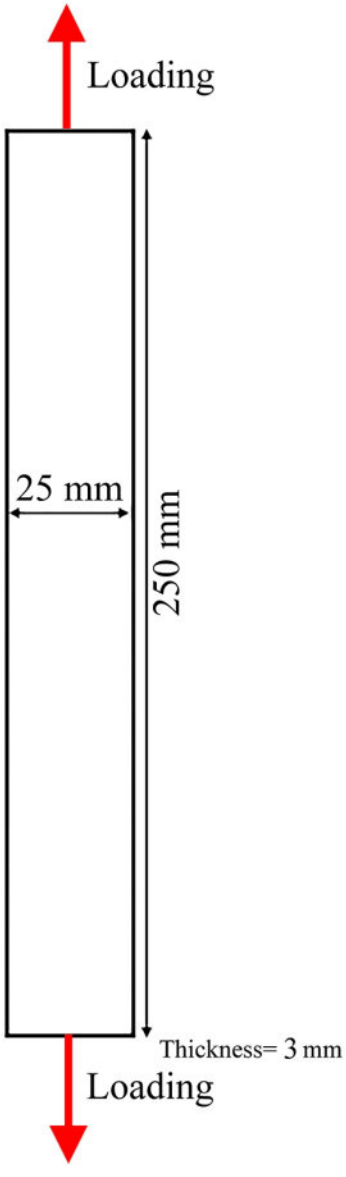

Drawing

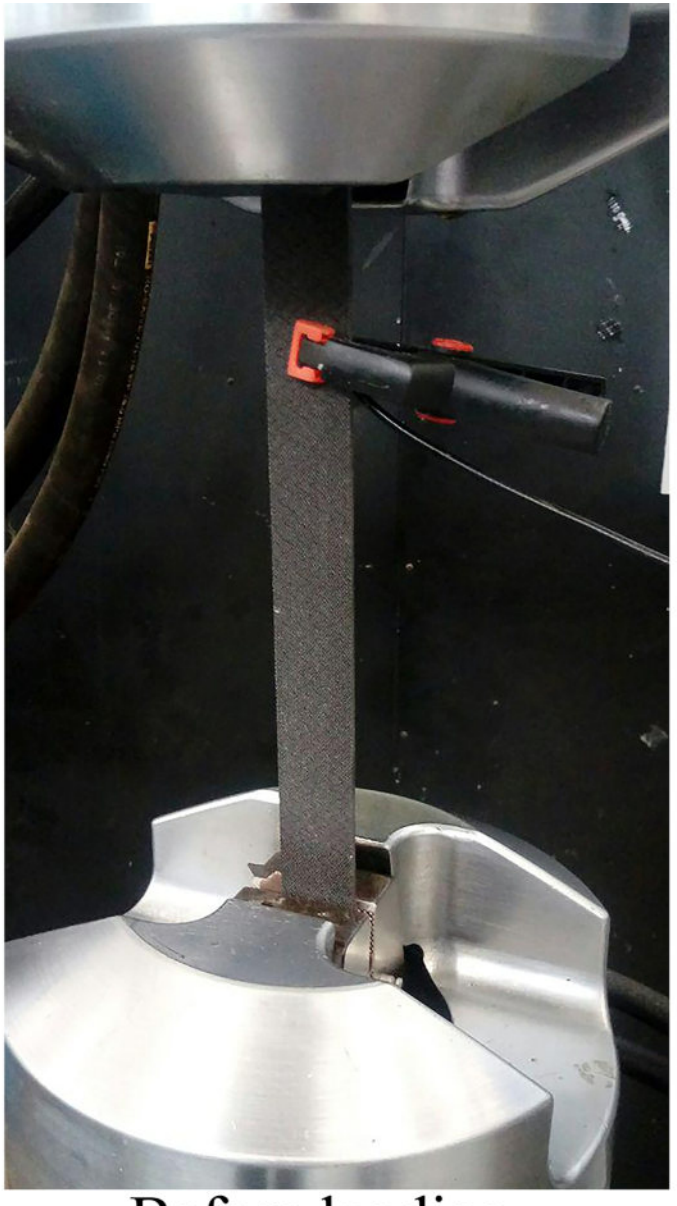

Before loading

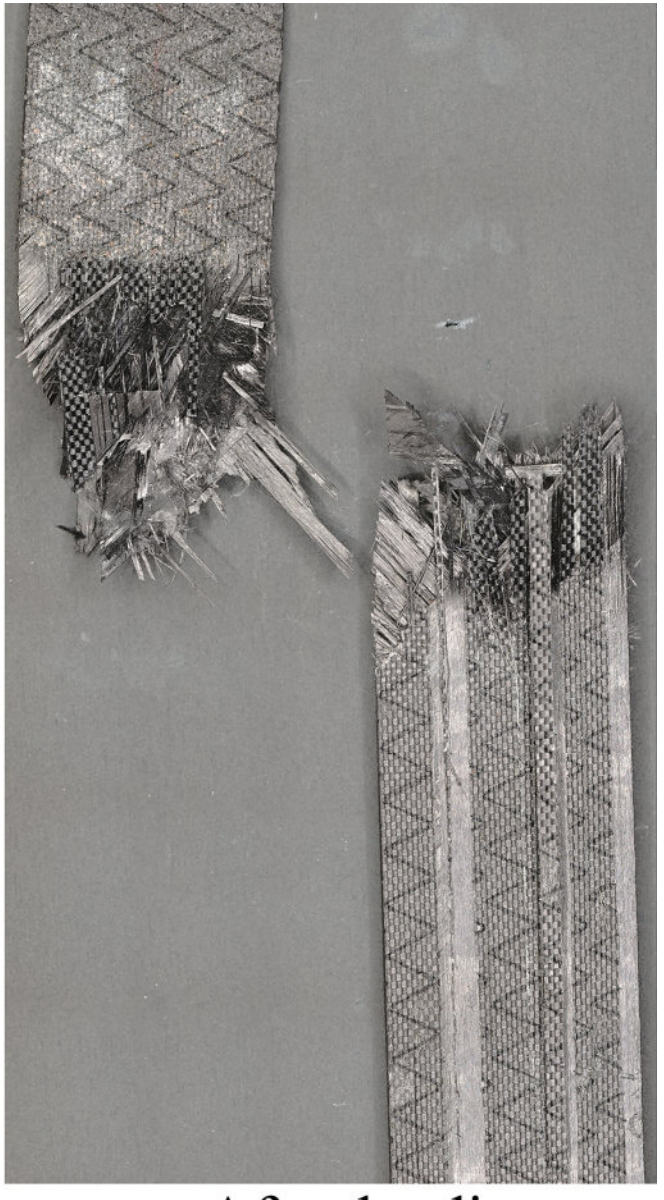

After loading

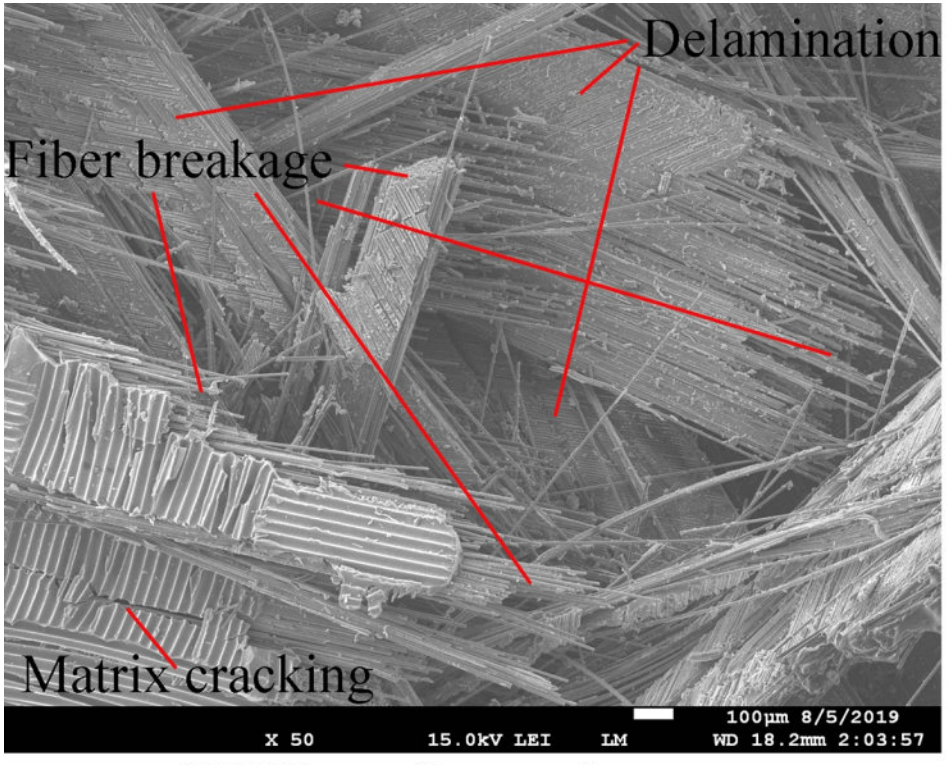

CFRP tensile specimen

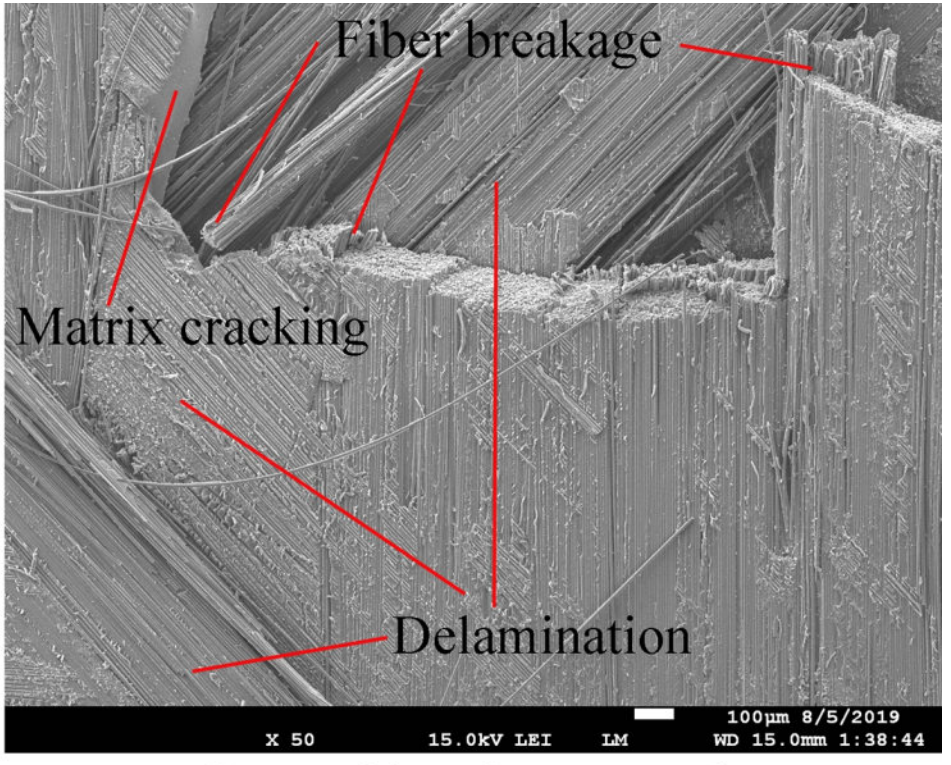

CFRP skin of DLJ specimen

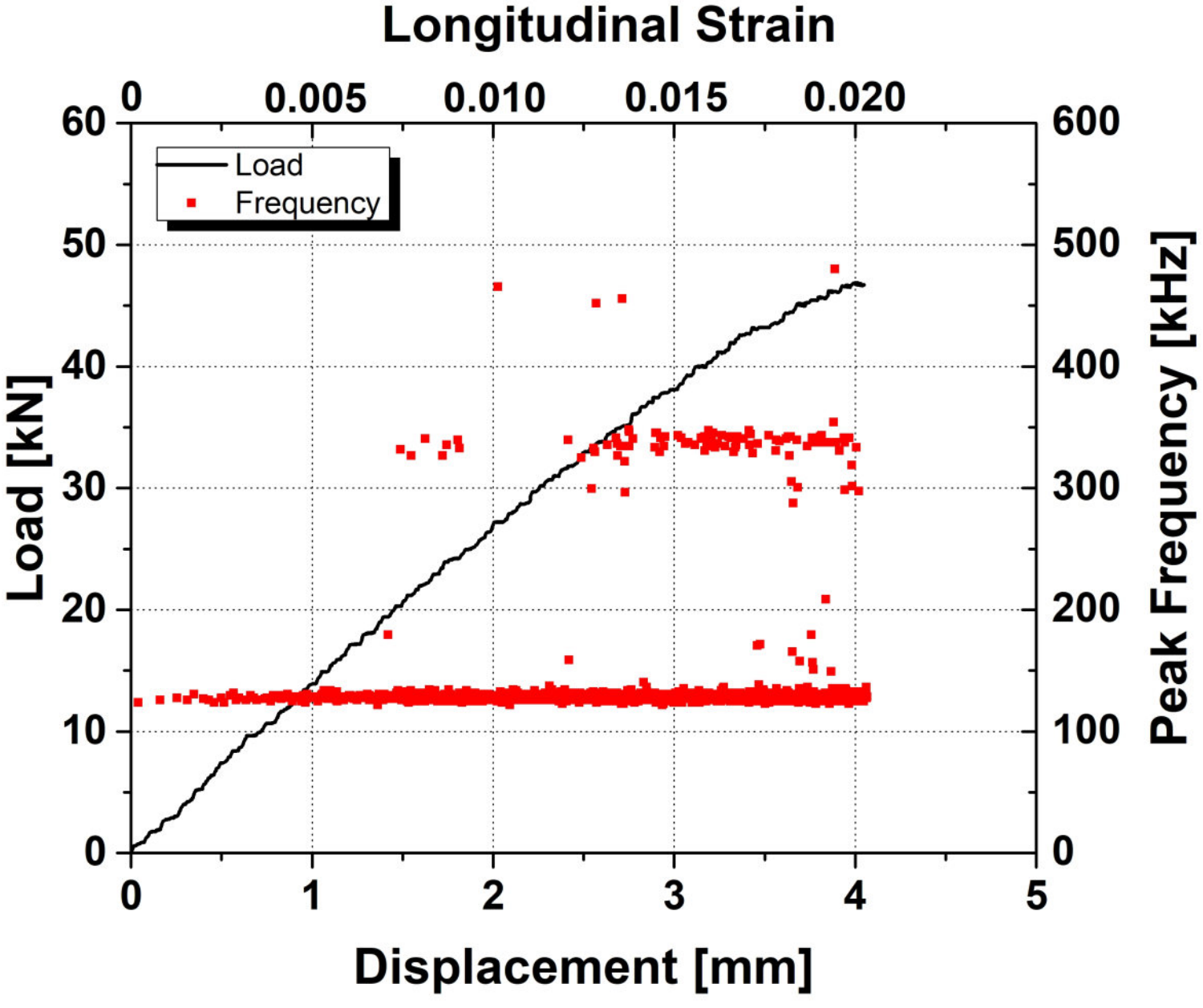
Longitudinal Strain
0
0.005
0.010
0.015
0.020
Load
Frequency
Load [kN]
Peak Frequency [kHz]
Displacement [mm]
0
10
20
30
40
50
60
0
100
200
300
400
500
600
0
1
2
3
4
5

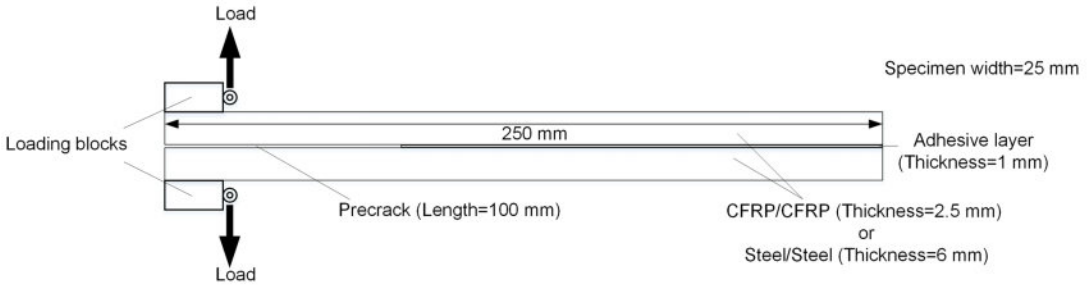
Load
Specimen width=25 mm
Loading blocks
250 mm
Adhesive layer
(Thickness=1 mm)
Precrack (Length=100 mm)
CFRP/CFRP (Thickness=2.5 mm)
or
Steel/Steel (Thickness=6 mm)
Load

(a)

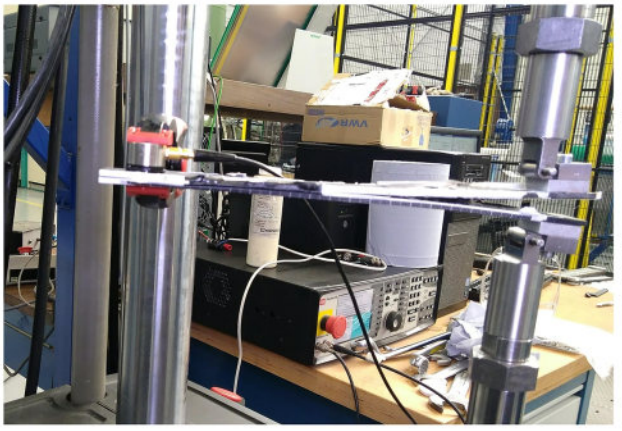

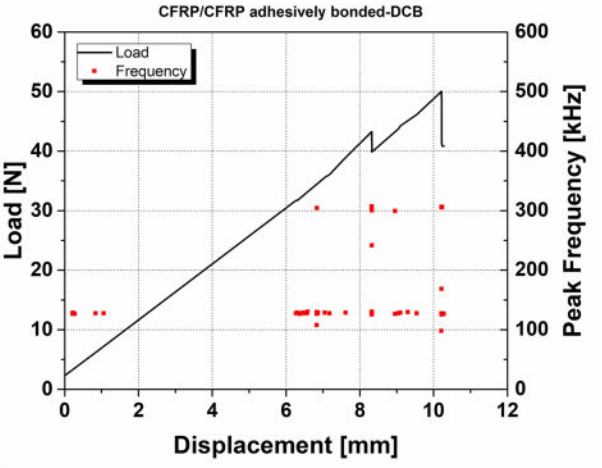
CFRP/CFRP adhesively bonded-DCB
Load
Frequency
Load [N]
Peak Frequency [kHz]
Displacement [mm]
0
10
20
30
40
50
60
0
100
200
300
400
500
600
0
2
4
6
8
10
12

(b)

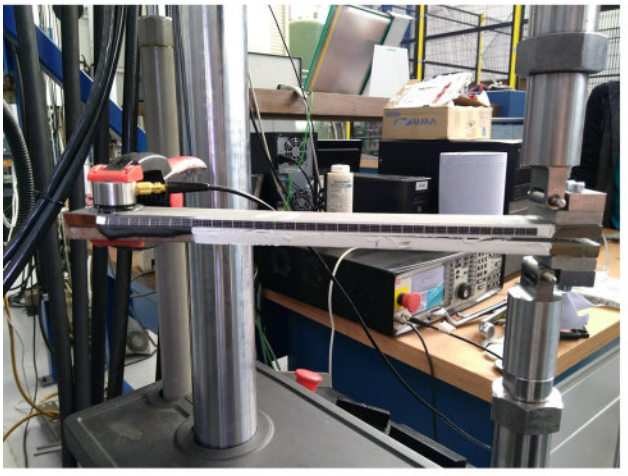

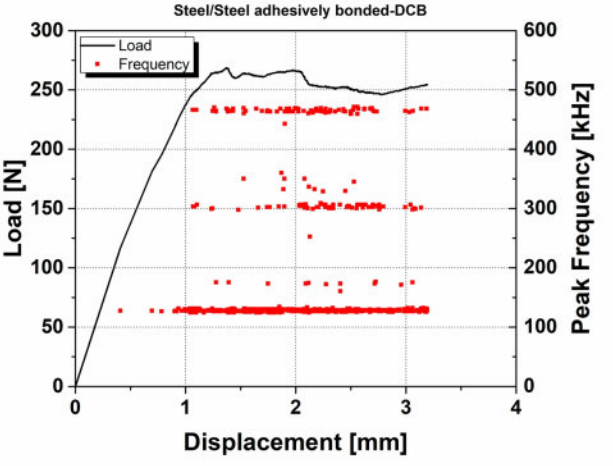
Steel/Steel adhesively bonded-DCB
Load
Frequency
Load [N]
Peak Frequency [kHz]
Displacement [mm]
0
50
100
150
200
250
300
0
100
200
300
400
500
600
0
1
2
3
4

(c)

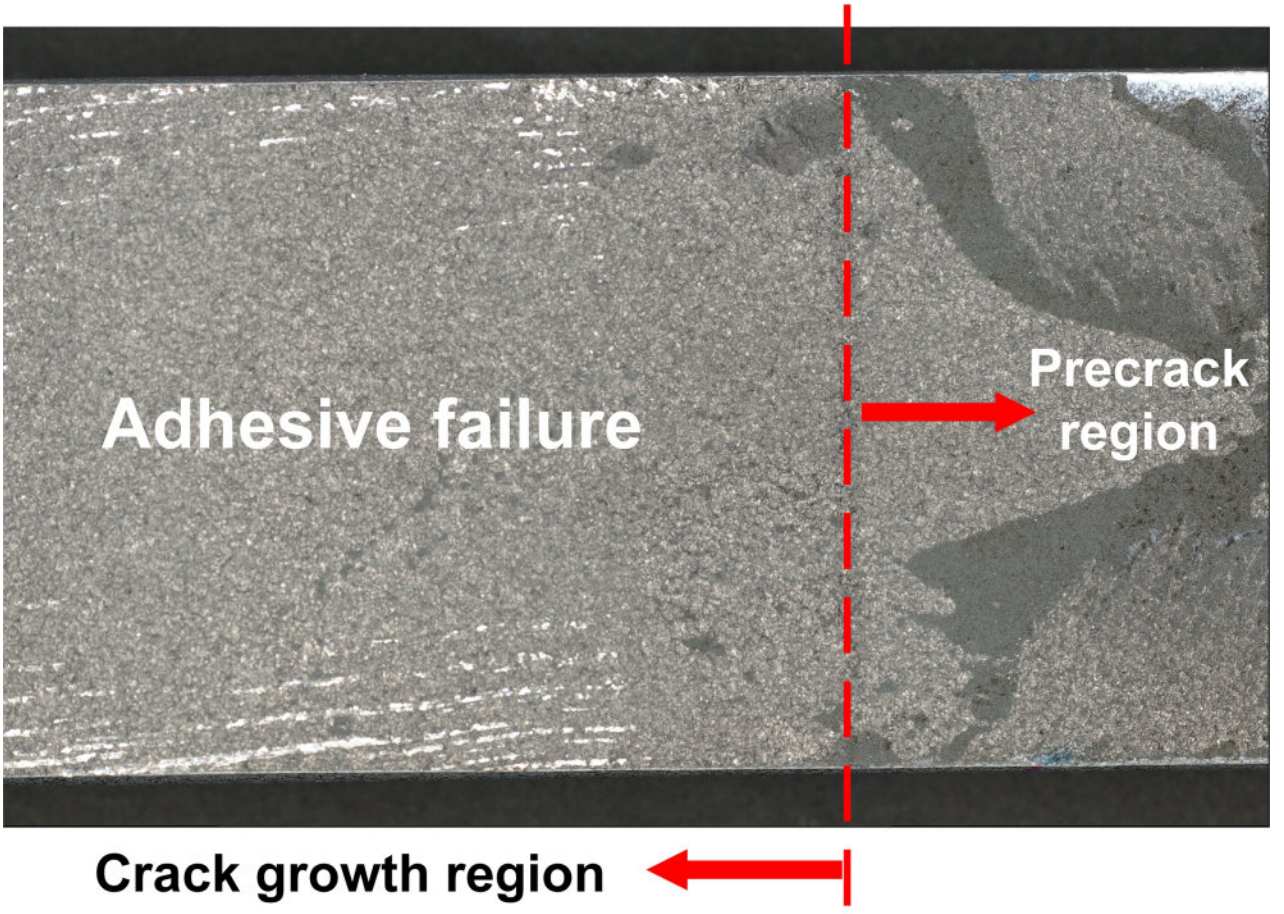
Adhesive failure
Precrack region
Crack growth region

(a)

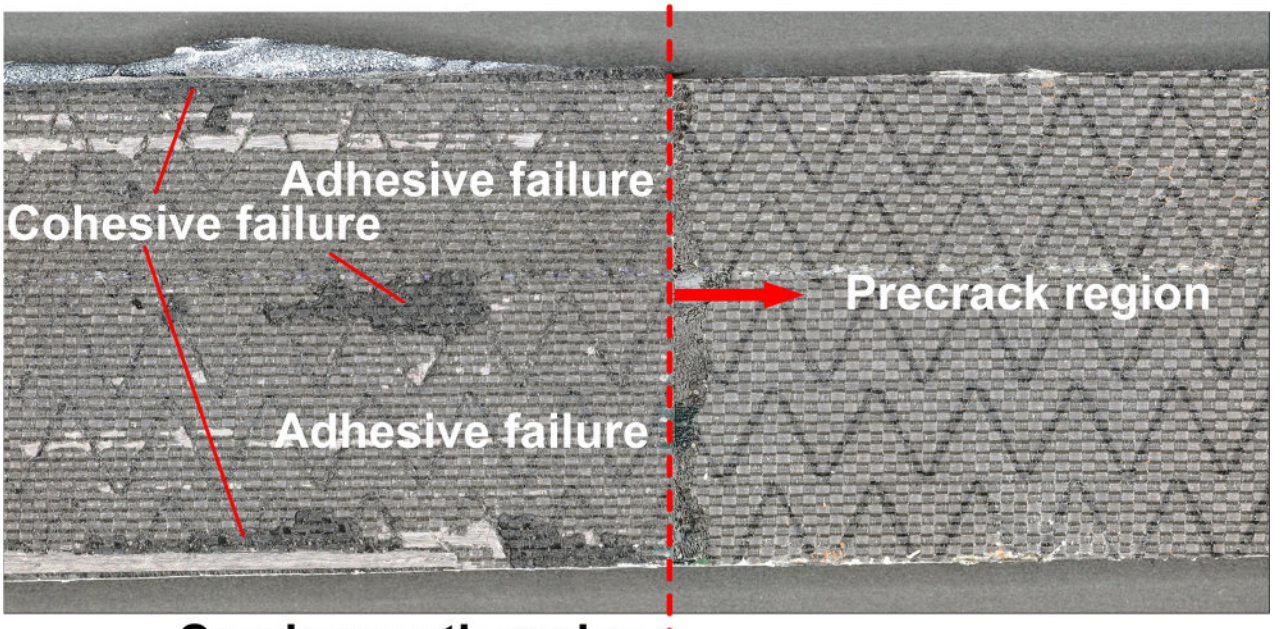
Adhesive failure
Cohesive failure
Precrack region
Adhesive failure
Crack growth region

(b)

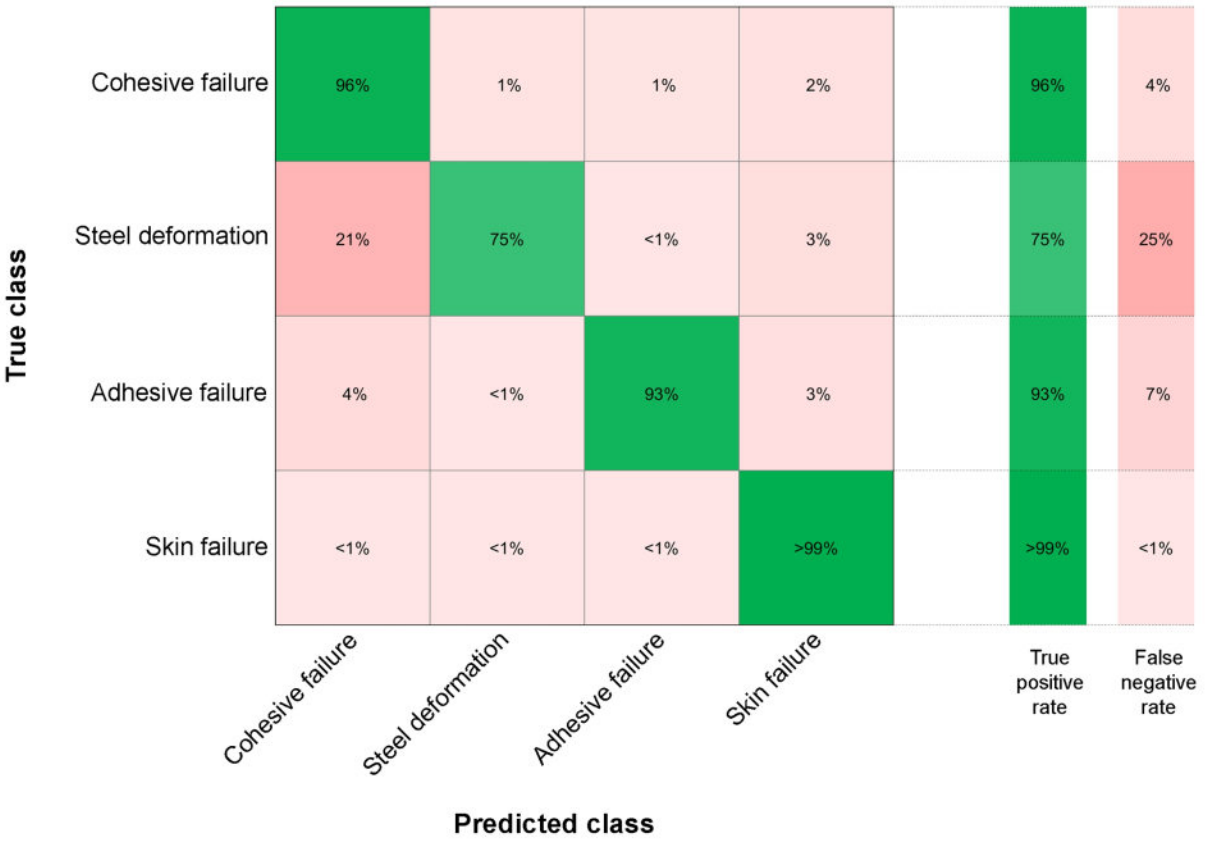
True class
Cohesive failure
Steel deformation
Adhesive failure
Skin failure
96%
1%
1%
2%
21%
75%
<1%
3%
4%
<1%
93%
3%
<1%
<1%
<1%
>99%
96%
75%
93%
>99%
4%
25%
7%
<1%
Cohesive failure
Steel deformation
Adhesive failure
Skin failure
True positive rate
False negative rate
Predicted class

(a)

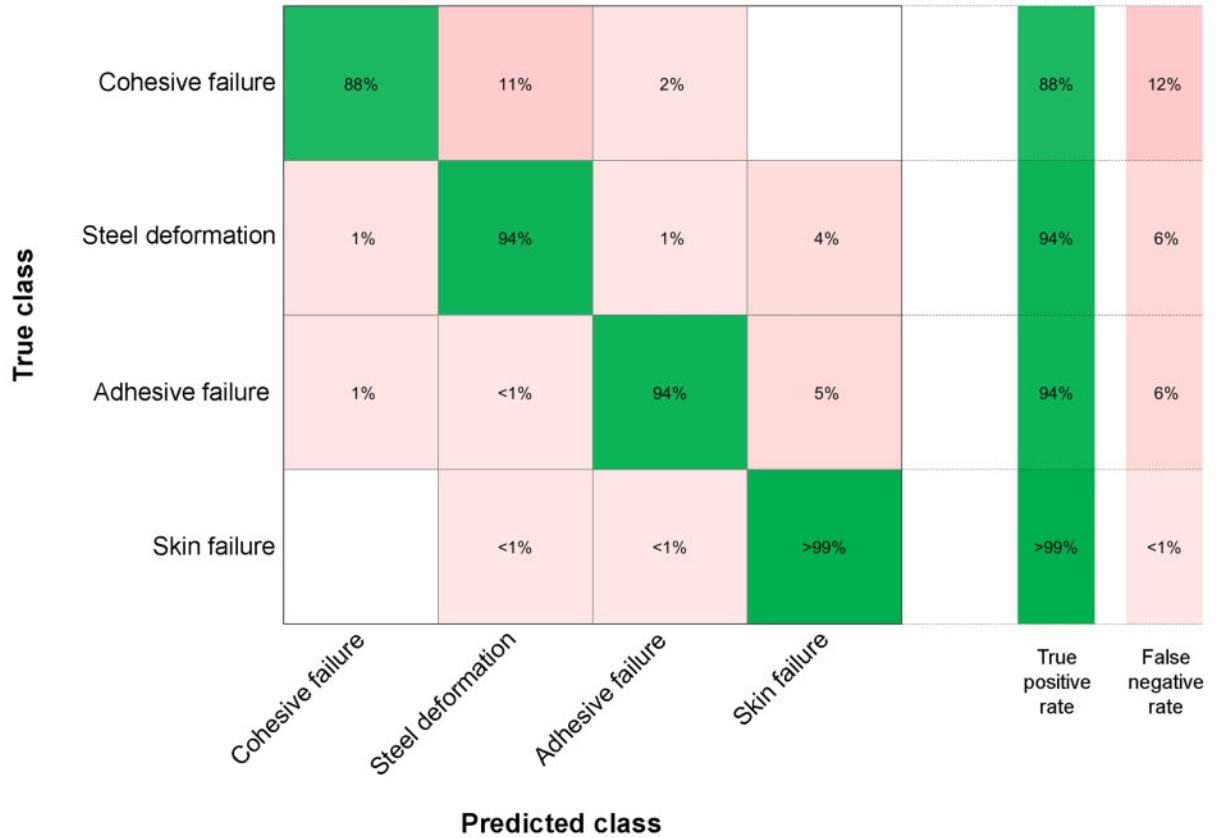
True class
Cohesive failure
Steel deformation
Adhesive failure
Skin failure
88%
11%
2%
1%
94%
1%
4%
1%
<1%
94%
5%
<1%
<1%
>99%
88%
94%
94%
>99%
12%
6%
6%
<1%
Cohesive failure
Steel deformation
Adhesive failure
Skin failure
True positive rate
False negative rate
Predicted class

(b)

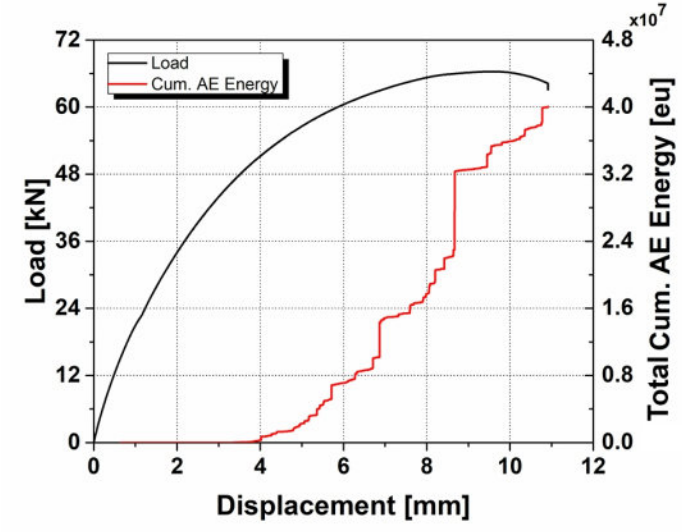

Classified damages

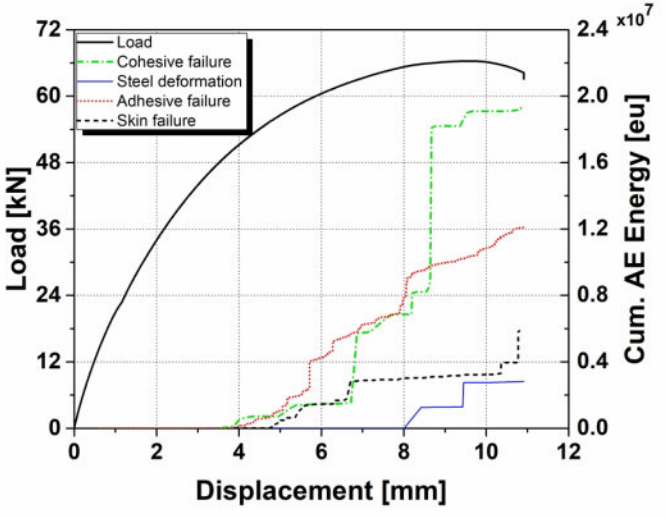

(a)

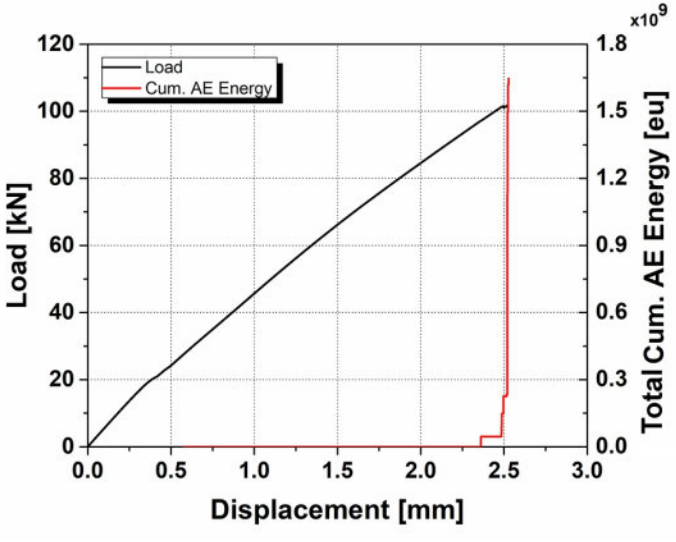

Classified damages

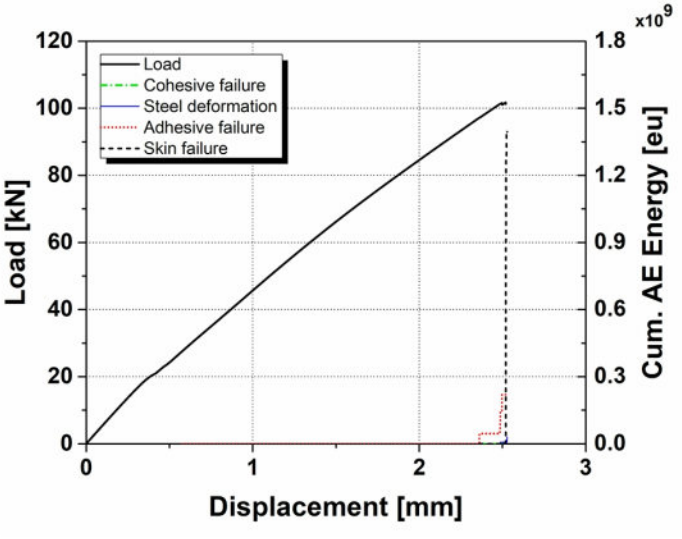

(b)

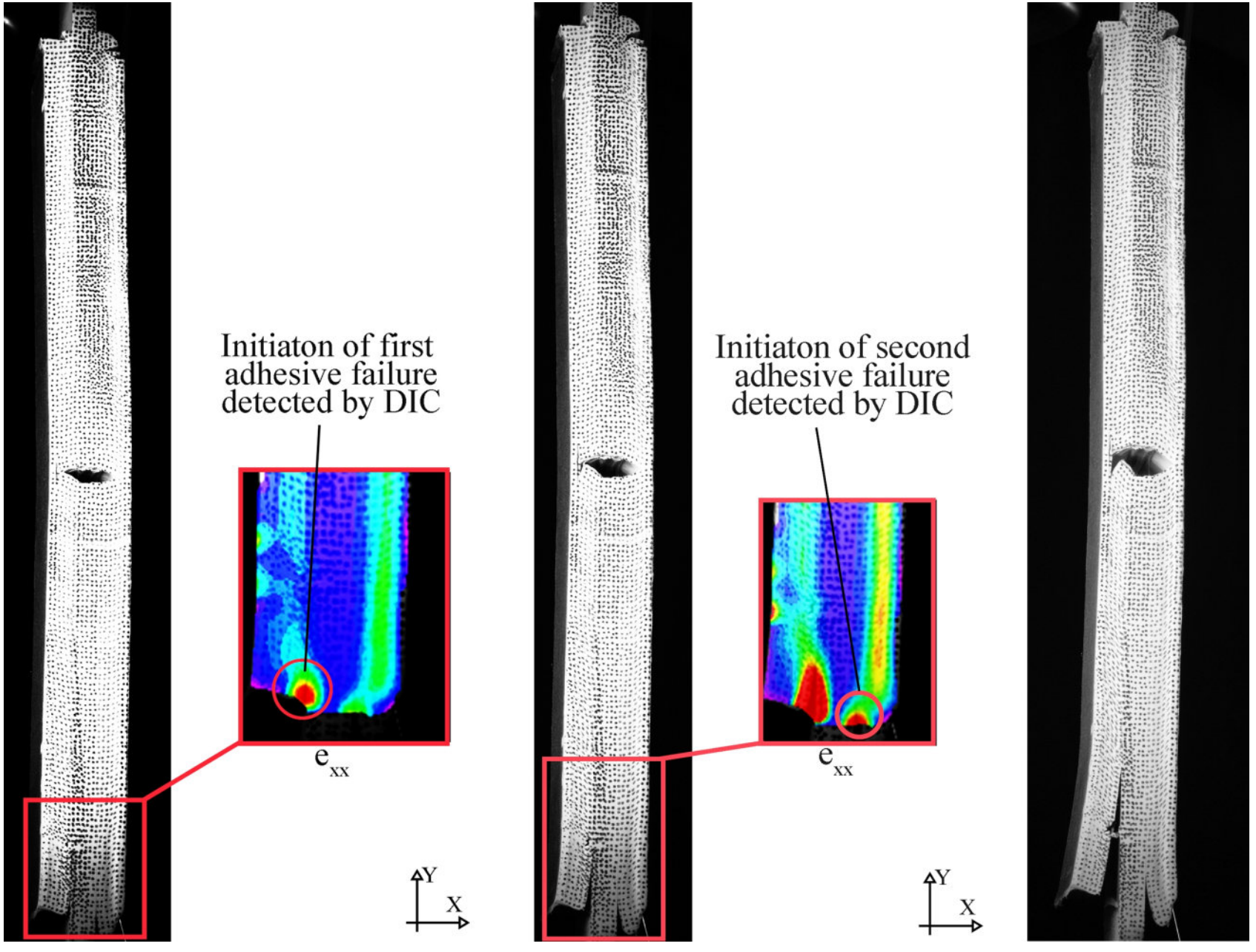
Initiaton of first
adhesive failure
detected by DIC
e_{xx}
Y
X
Initiaton of second
adhesive failure
detected by DIC
e_{xx}
Y
X

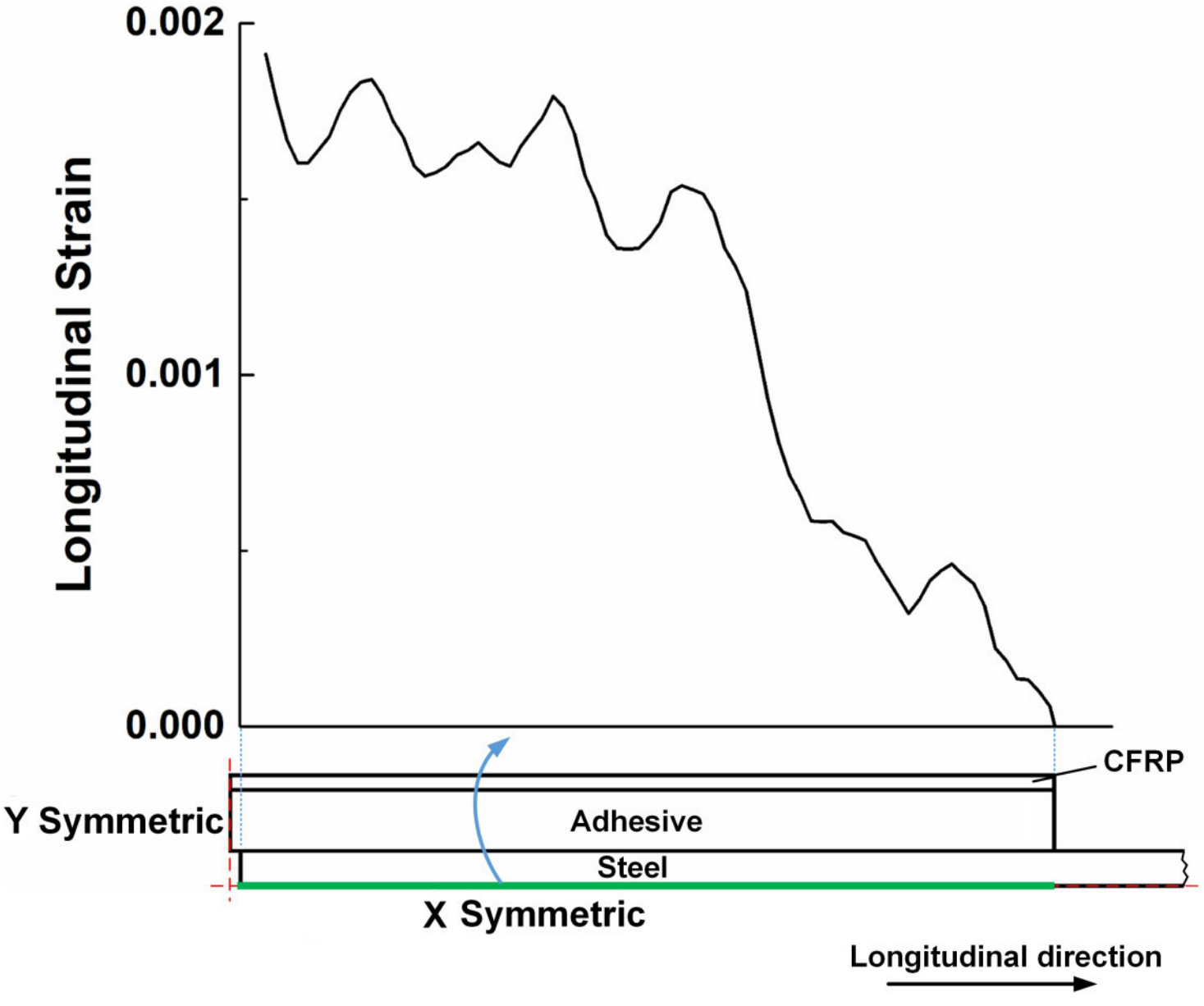
0.002
0.001
0.000
Longitudinal Strain
CFRP
Adhesive
Steel
Y Symmetric
X Symmetric
Longitudinal direction

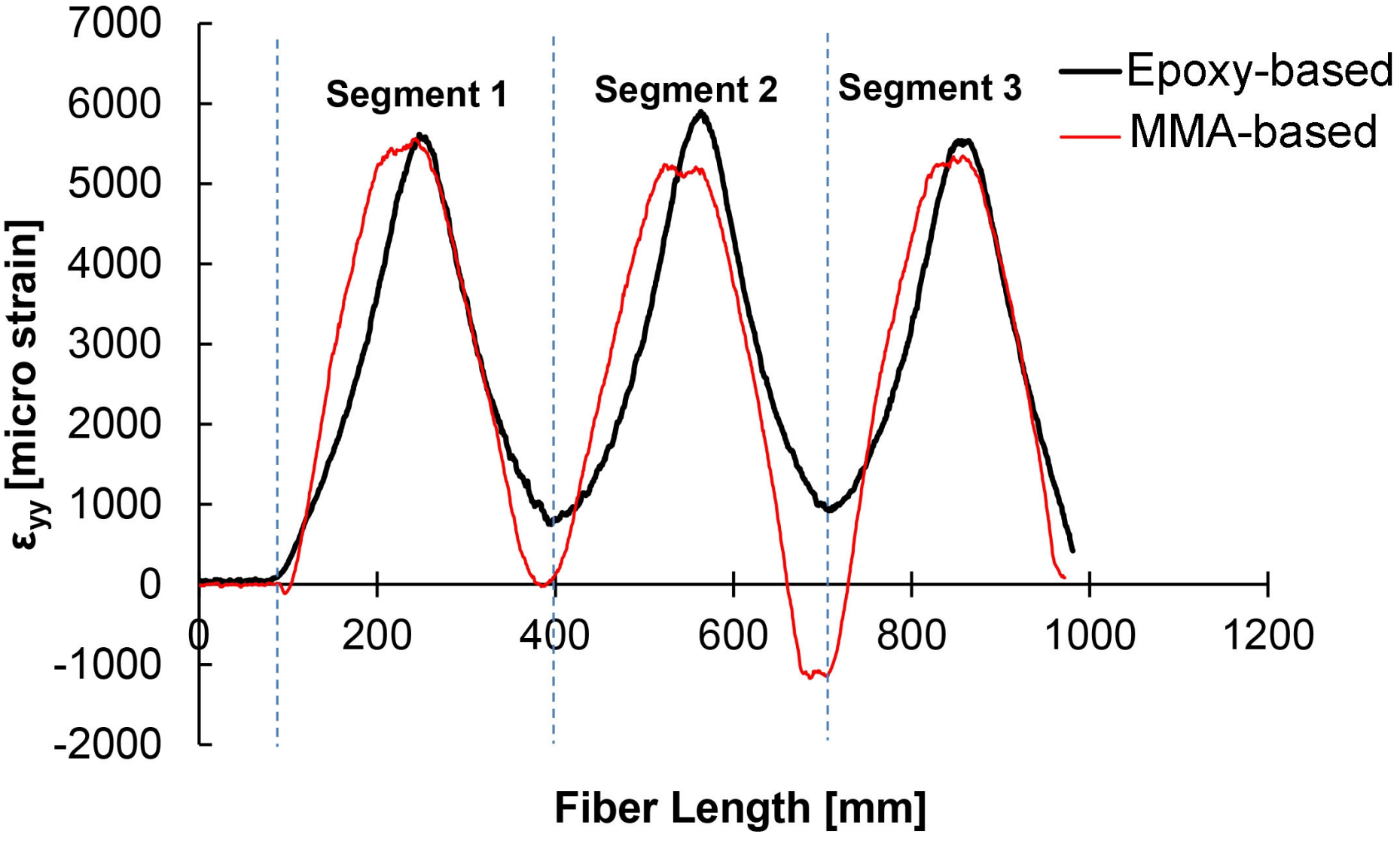
7000
6000
5000
4000
3000
2000
1000
0
-1000
-2000
ε_{yy} [micro strain]
Segment 1
Segment 2
Segment 3
Epoxy-based
MMA-based
0
200
400
600
800
1000
1200
Fiber Length [mm]

Table 1. Mechanical properties of the constituent materials.

Parameter	Steel	MMA-based adhesive	Epoxy-based adhesive
Tensile modulus (GPa)	200	0.20	2
yield strength (MPa)	350	-	-
ultimate strength (MPa)	400-550	12-15	37
Poisson's ratio	0.26	-	-
Strain to failure (%)	-	40-60	10.10

Table 2. The specifications of the individual constituent tests.

Material	Type of test	Standard	The corresponding damage in the DLJ test
Steel	Tensile	ASTM E8 [30]	Plastic deformation of steel core
	Shear	ASTM B831-14 [31]	
Adhesive	Tensile	ASTM D638 – 14 [32]	Plastic deformation of adhesive part (Cohesive failure)
	Mode I	Reference [33]	Crack growth in the adhesive under mode I (Cohesive failure)
	Mode II	Reference [33]	Crack growth in the adhesive under mode II (Cohesive failure)
Steel/Steel adhesively-bonded DCB	Mode I	ASTM D5528 [34]	Adhesive failure at steel/adhesive interface
CFRP/CFRP adhesively-bonded DCB	Mode I	ASTM D5528 [34]	Adhesive failure at CFRP/adhesive interface
CFRP	Tensile	ASTM D3039 [35]	Damage of the CFRP skins

Table 3. The specification of the training data for the ensemble decision tree classifier.

Material	Test	Label	AE signals Number
Adhesive	Tension	Cohesive failure	11269
	Mode I		
	Mode II		
Steel	Tension	Steel deformation	1771
	Shear		
Steel/Steel and CFRP/CFRP adhesively-bonded	DCB	Adhesive failure	3513
CFRP	Tension	Skin failure	209638